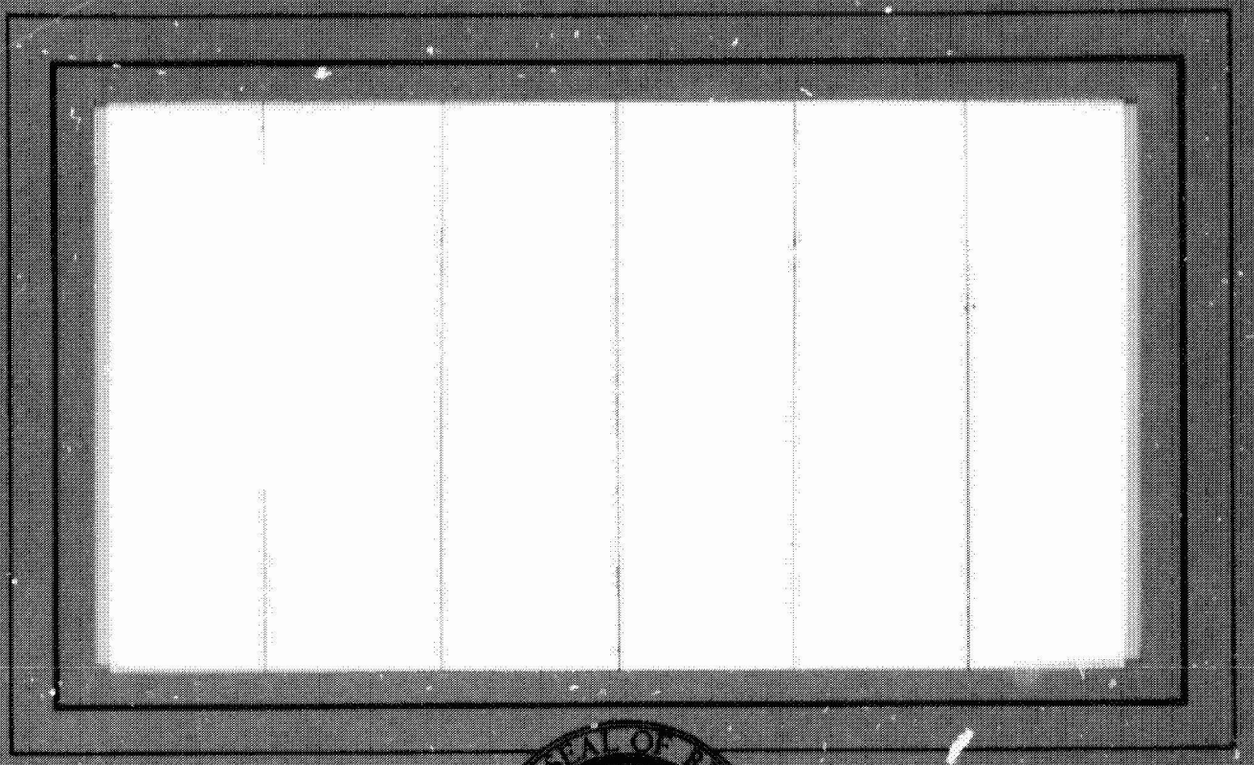

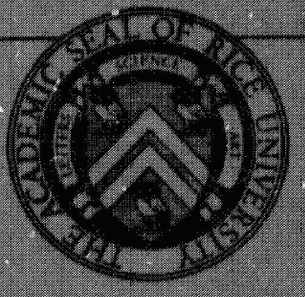


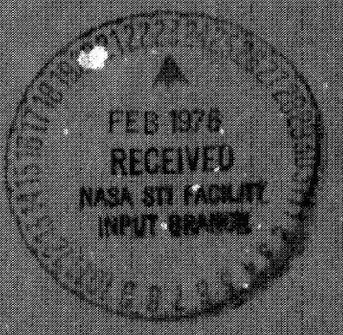


DEPARTMENT OF

# SPACE PHYSICS

AND

# ASTRONOMY

## RICE UNIVERSITY

HOUSTON, TEXAS 77001

(NASA-CR-146413) A PROGRAM OF DATA SYNTHESIS FROM THE ALSEP/CPLEE ALSEP/SIDE, AND EXPLORER 35 MAGNETOMETER TO INVESTIGATE LUNAR TERMINATOR AND NIGHTSIDE PARTICLE FLUXES AND SURFACE INTERACTIONS Final (Rice G3/91

N76-18017

HC $4.50

Unclas 14132

FINAL TECHNICAL REPORT

NSG-07025

# A Program of Data Synthesis from the ALSEP/CPLEE ALSEP/SIDE, and Explorer 35 Magnetometer to Investigate Lunar Terminator and Nightside Particle Fluxes and Surface Interactions.

Submitted to the

National Aeronautics and Space Administration

by

Rice University
Houston, Texas

February 2, 1976

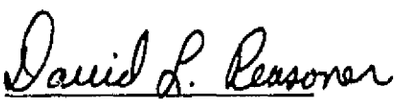

David L. Reasoner

Table of Contents


| | | Page |
|---|---|---|
| I. | Summary | 3 |
| II. | Introduction | 5 |
| III. | Instruments and Data Base | 7 |
| IV. | Scientific Results | 9 |
| V. | Conclusions | 33 |
| VI. | Acknowledgments | 34 |
| VII. | References | 35 |
| | Appendix A - List of Scientific Publications | 37 |
| | Appendix B - Abstracts and Reprints | 39 |

## Summary

This is the final technical report on the Lunar Data Analysis and Synthesis Program Grant No. NSG-07025 awarded to Rice University by the Lunar Programs Office of the National Aeronautics and Space Administration. The purpose of the research was to use data from the ALSEP/CPLEE instrument along with other lunar-surface and lunar-orbiting instruments to study interactions between the moon and its space plasma environment.

Principal research accomplishments under this grant were:

1. Study of lunar nightside electron fluxes and identification of three distinct classes of flux events. The events were shown to be due to a) electrons propagating upstream from the earth's bow shock; b) electrons thermalized and scattered to the lunar surfac by disturbances along the boundary of the lunar solar-wind cavity; c) solar wind electrons scattered to the lunar surface by lunar limb shocks and/or compressional disturbances.
2. Identification of these lunar nightside electrons as a causative agent of the high night surface negative potentials observed in the ALSEP/SIDE ion data.
3. Study of the shadowing of magnetotail plasma sheet electrons by interactions between the lunar body and the ambient magnetic field and by interactions between charged particles and the lunar remnant magnetic fields in the vicinity of the instrument. These shadowing effects were shown to have important effects in modification of the lunar-surface and near-lunar potential distributions.

These studies will be described in detail in this report.

The NASA Technical Officer for this grant is Dr. Desiree Stuart-Alexander, Code SM, NASA Lunar Programs Office.

## Introduction

The Charged Particle Lunar Environment Experiment (CPLEE) was deployed on the lunar surface during the Apollo 14 mission on February 6, 1971. Over a lifetime of approximately 2 1/2 years the instrument returned much valuable data concerning the charged particle environment of the moon and the interactions between space plasmas and the lunar body and surface. The initial hardware and data analysis contract (NAS9-5884) continued until March 1974 and the final report for that contract contains the scientific justification, instrument description, and scientific research activity of the CPLEE program up to that time. Briefly, the initial period of data analysis concentrated upon analysis and understanding of charged particle fluxes to the dayside lunar surface. We investigated the lunar surface photoelectron layer, the properties of the plasma sheet in the geomagnetic tail at lunar distance, properties of magnetosheath particle populations, relations between charged particle events observed at the moon and events observed closer to the earth by other satellites, and changes in the magnetotail geometry during magnetic storms. Other investigations included particle fluxes due to artificial lunar surface impact events and cosmic ray particles from the August 1972 solar flares. The reader should refer to the NAS9-5884 final report for a complete bibliography.

In our studies of CPLEE data, it became obvious that many of the phenomena observed were not an intrinsic feature of the lunar environment but rather were the result of interactions between the moon and its space plasma environment. One such

example is the layer of photoelectrons which forms on the sunlit lunar surface and which creates a positive surface potential ranging up to 200 volts (Reasoner and Burke, 1972). Significant fluxes of electrons were observed throughout the lunar night when the moon was upstream of the earth in the solar wind and the CPLEE instrument was viewing into the downstream lunar wake cavity. That any fluxes were observed at all was indeed surprising, for previous models of lunar-solar wind interactions predicted that the cavity should be empty of plasma.

The Post-Apollo Data Analysis and Synthesis Program afforded an opportunity to make a study of plasma-lunar interactions using data from the CPLEE instrument, the ALSEP/SIDE instrument, and the Explorer 35/Ames Research Center Magnetometer in lunar orbit. We proposed to make such a study and the grant was awarded in March 1974. A one-year extention was granted in March 1975.

The scientific reports and publications are listed in Appendix A. One student, Dr. Patricia H. Reiff, received her Ph.D. degree from research conducted under this grant.

## Instruments and Data Base

Data from the ALSEP/CPLEE (primary), the Apollo 14 ALSEP/SIDE, and the Explorer 35/ARC Magnetometer were used in these studies. The ALSEP/SIDE data were supplied by Dr. J. W. Freeman, Jr., of Rice University. Data from the Explorer 35 Magnetometer had been supplied to us earlier by Dr. D. S. Colburn of Ames Research Center, and we continued to use the data in these studies.

The CPLEE and SIDE instruments have been described extensively in other publications. See, for example, the Apollo 14 Preliminary Science Report, NASA SP-272. Briefly, the CPLEE instrument is an ion-electron spectrometer which covers the energy range 40 eV - 20,000 eV in 15 steps. The instrument contains two identical analyzers, one looking toward local lunar vertical (Analyzer A) and the other looking 60° from local vertical toward lunar west (Analyzer B). The CPLEE completes a complete measurement cycle in 19.2 seconds. The SIDE instrument contains an ion energy analyzer covering the energy range 10 - 3500 eV in 20 steps with a cycle time of approximately 1.5 minutes. The instrument also contains a mass analyzer, but no mass analyzer data were used in these studies.

The Explorer 35/ARC Magnetometer is a three-axis instrument with a basic resolution of 0.125 $\gamma$ (1 $\gamma = 10^{-5}$ Gauss). The data were supplied to us in the form of digital magnetic tapes containing 82 second averages of the magnetic field values.

Other ancillary data included solar wind conditions and the geomagnetic activity index Kp from archived sources of the National Space Science Data Center and published data from the Lunar Portable Magnetometer Experiment (Dyal, et al., 1971).

## Scientific Results

In this section we discuss the scientific results of the CPLEE Post-Apollo Data Analysis and Synthesis Program. As this report contains reprints of many of the scientific publications, only summaries will be presented here.

I. Lunar Night Electron Fluxes

Figure 1 shows an example of the data which motivated this study. The counting rates due to 200 eV electrons are plotted as a function of time for a period around lunar sunset. The exact time of sunset (terminator crossing) is marked by the vertical arrow. The relative high, stable fluxes during the first part of the period are lunar surface photoelectrons (Reasoner and Burke, 1972). As the solar illumination angle increases, the photoelectron fluxes decrease (hour 4 of day 49) and the fluxes between this time and lunar sunset are a mixture of photoelectrons and solar wind electrons, which tend to be more erratic in nature. However, in contrast to classical predictions the electron fluxes do not vanish at sunset but rather persist long after sunset. In fact, as will be seen in subsequent figures, sporadic through significant fluxes persist throughout the lunar night. Solar wind aberration (the shift in the solar wind direction caused by the motion of the earth-moon system through the interplanetary medium) could account for fluxes persisting up to ∿12 hours following terminator crossing, but the effect would be asymmetrical relative to the dawn and dusk terminators. In fact, no such effect could be discerned; that is, the fluxes displayed no preference toward either terminator.

Figure 1

An example of electron flux data observed near lunar sunset. Sunset is marked by the vertical arrow. It is seen that significant fluxes persist long after sunset.

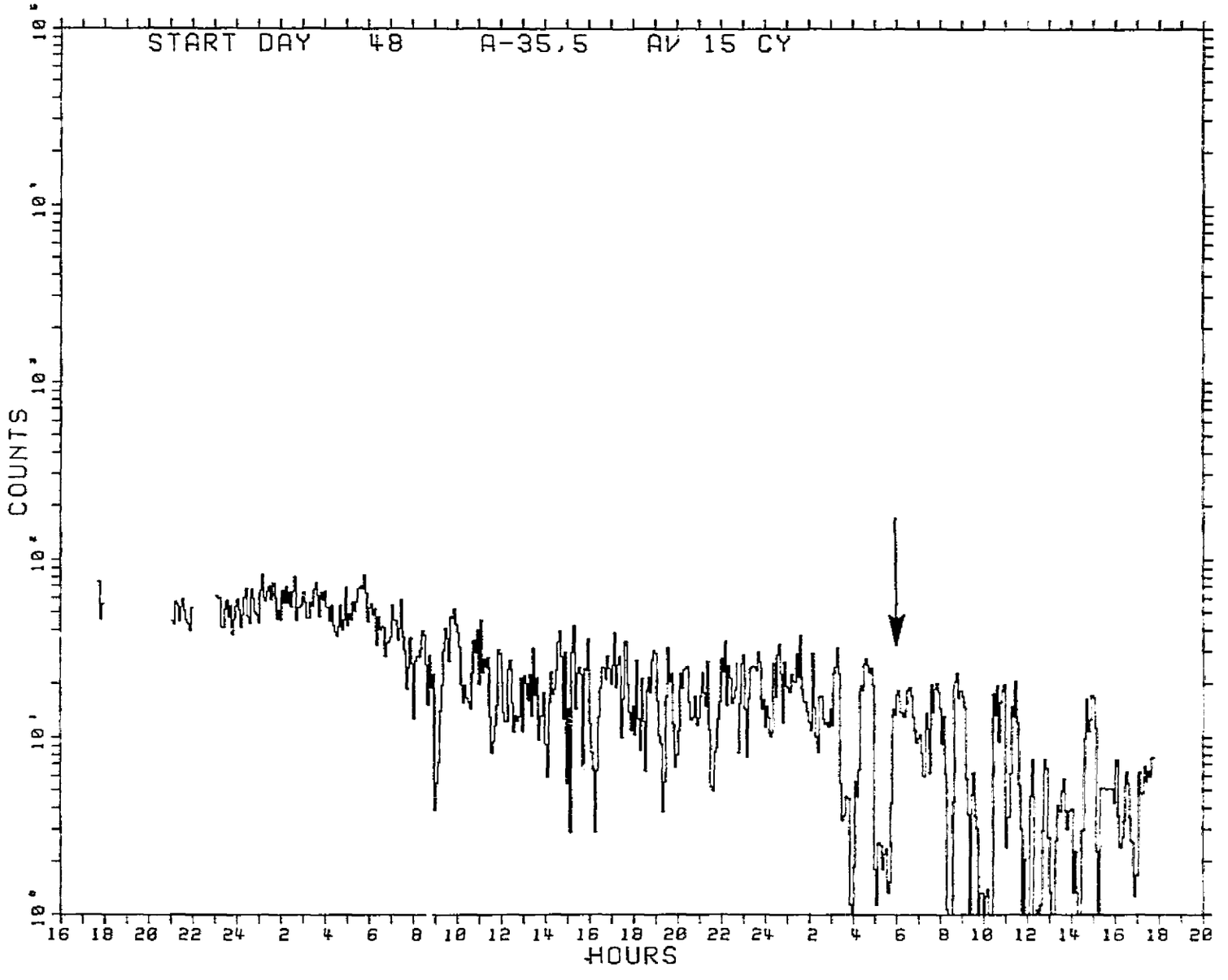
START DAY 48 A-35,5 AV 15 CY
COUNTS
HOURS
16 18 20 22 24 2 4 6 8 10 12 14 16 18 20 22 24 2 4 6 8 10 12 14 16 18 20

Figure 2 is an example (bottom panel) of fluxes observed near lunar midnight. The top two panels show the latitude $\theta$ and the longitude $\phi$ of the interplanetary magnetic field measured with the Explorer 35/AKC Magnetometer. The data gaps in the magnetometer record are due to the operational characteristics of the Explorer 35 Satellite. It was observed, in a study of 4 months of data, that there seemed to be preferred directions of the IMF for the occurrence of some of the fluxes. The preferred directions seemed to be near a line connecting the earth to the moon. Accordingly, a model of the earth's bow shock surface was constructed (a hyperboloid of revolution) and for each position of the moon the zone in $\theta - \phi$ space where the IMF would connect the moon to the bow shock were computed. The dotted line on the $\phi$ plot represents the boundaries of the IMF earth-moon connection zone. The zone boundary lines are irregular since the width of the zone in $\phi$ is a function of the latitude $\theta$. We see that the electron fluxes are significantly larger whenever $\phi$ falls into the connection zone (e.g., at 0215-0230 and 0305-0405). In all, 14 such events were identified in the data set. There were undoubtedly more, but could not be uniquely identified because of missing magnetometer data. The flux events which are correlated with IMF direction were labeled Type I and the other, lower intensity events were labeled Type II. The Type I events therefore must originate at the earth's bow shock and propagate back upstream in the solar wind to impact the nightside lunar surface. We will return to the Type II events later.

Figure 2

Examples of Type I and Type II lunar night flux events. The lower panel is the counting rate due to 200 eV electrons and the top two panels are the latitude $\theta$ and longitude $\phi$ of the IMF. The dotted lines on the $\phi$ plot show the zones where the IMF connects the moon to the earth's bow shock. The higher intensity Type I events are seen to occur only when $\phi$ is within the connection zones.

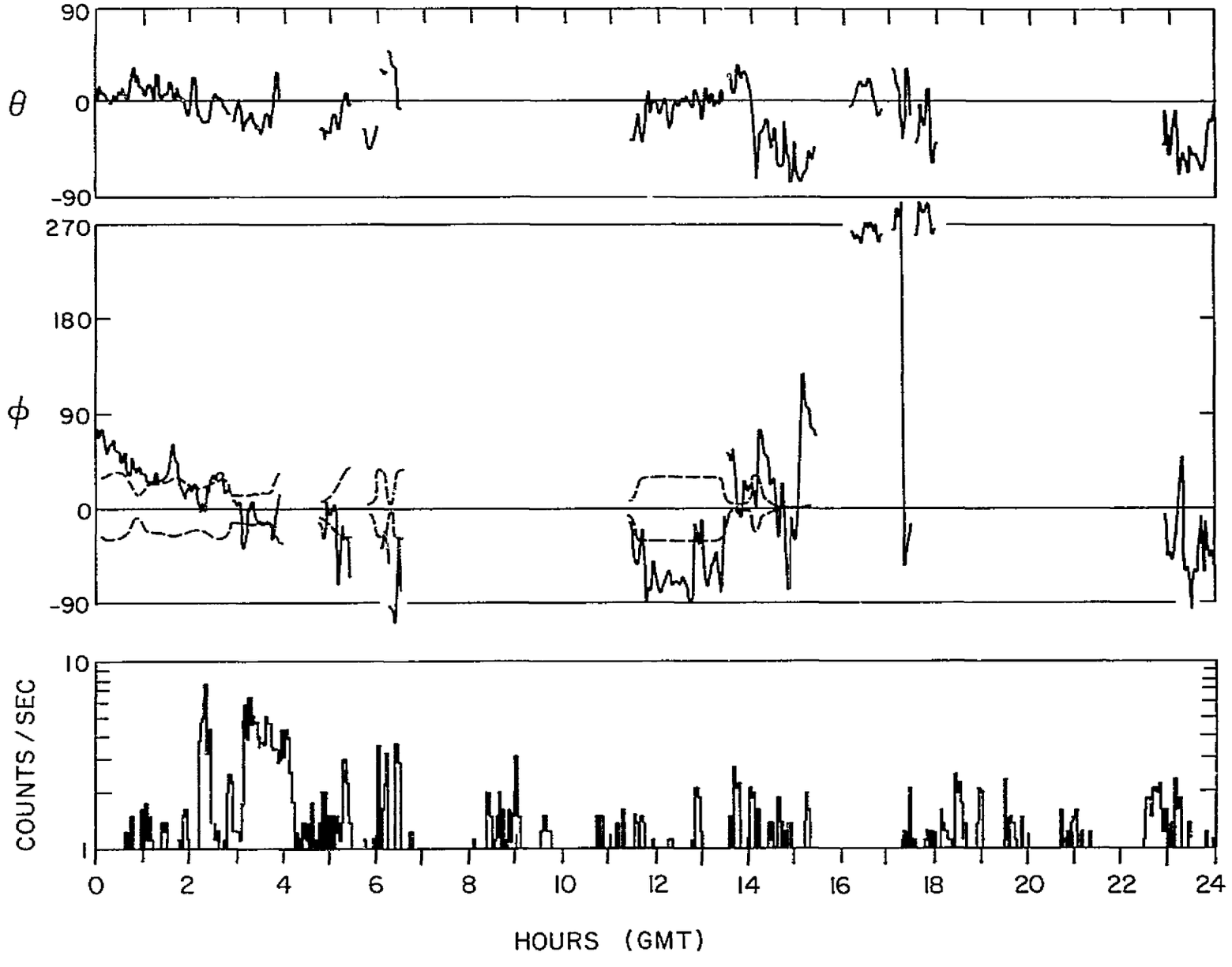
90
θ
0
-90
270
180
φ
90
0
-90
10
COUNTS / SEC
1
0
2
4
6
8
10
12
14
16
18
20
22
24
HOURS (GMT)

Scudder et al. (1973) reported observations of solar wind electron temperatures with OGO-5. They found that on the average the solar wind electron temperature was higher when the satellite was connected to the bow shock along IMF lines. They attributed the higher temperatures to a non-Maxwellian component with a temperature on the order of 100 eV. In Figure 3 is shown a superposition of a typical solar wind electron spectrum with a characteristic temperature of ~10 eV and a typical spectrum of a Type I event. It is seen that the addition of Type I fluxes to the solar wind electrons results in a flux enhancement at higher energies which would be interpreted as a solar wind electron temperature increase, but that the true nature of the additional flux would not be seen by a detector exposed to the direct solar wind. However, for this study the moon acted to shield the instrument from the direct solar wind and allowed an uncontaminated measure of these electrons.

Figure 4 shows an example of a third type of lunar nightside electron flux event. Here, as in Fig. 2, the counting rate of the 200 eV electron channel is displayed. Also shown is the geomagnetic disturbance parameter Kp. The data displayed cover the period from 1200 U.T. on May 18, 1971 (Day 138) to 0000 U.T. on May 23 (Day 143). Lunar sunset, marked by an arrow and the corresponding disappearance of lunar photoelectron fluxes, occurred at 1930 U.T. on May 18 (Day 138). Electron fluxes are seen at the terminator and to persist into the lunar night period for approximately 4 days but with gradually decreasing intensity. The corresponding behavior is also seen prior to dawn terminator

Figure 3

A composite spectrum of solar wind electrons and a Type I event, showing that the superposition of the two results in an apparent higher temperature for the solar wind electrons.

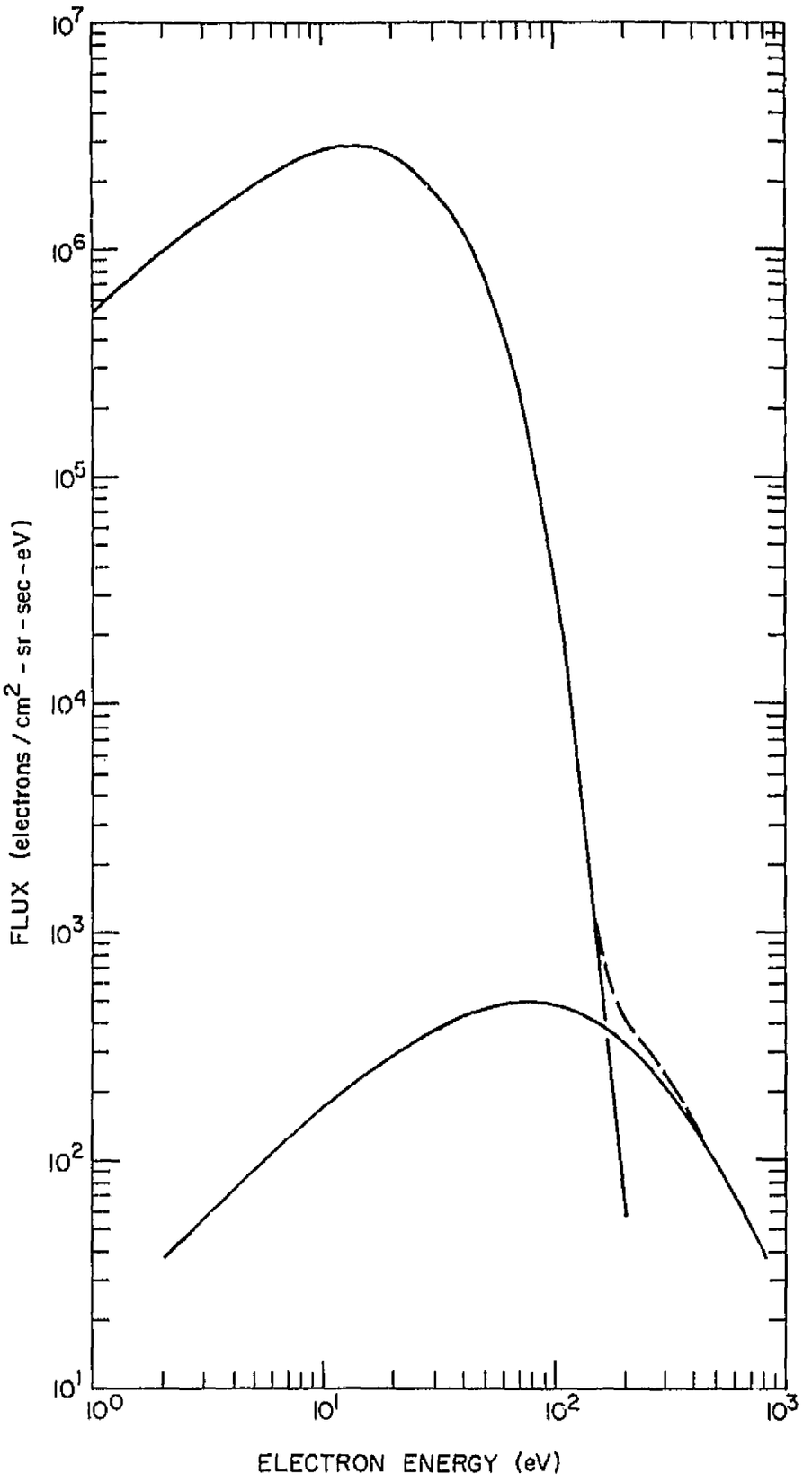
FLUX (electrons / cm$^2$ - sr - sec - eV)
$10^7$
$10^6$
$10^5$
$10^4$
$10^3$
$10^2$
$10^1$
$10^0$
$10^1$
$10^2$
$10^3$
ELECTRON ENERGY (eV)

Figure 4

Examples of Type III lunar night flux events, showing their correlation with distance from the lunar terminator (marked with the vertical arrow) and with the geomagnetic activity index Kp.

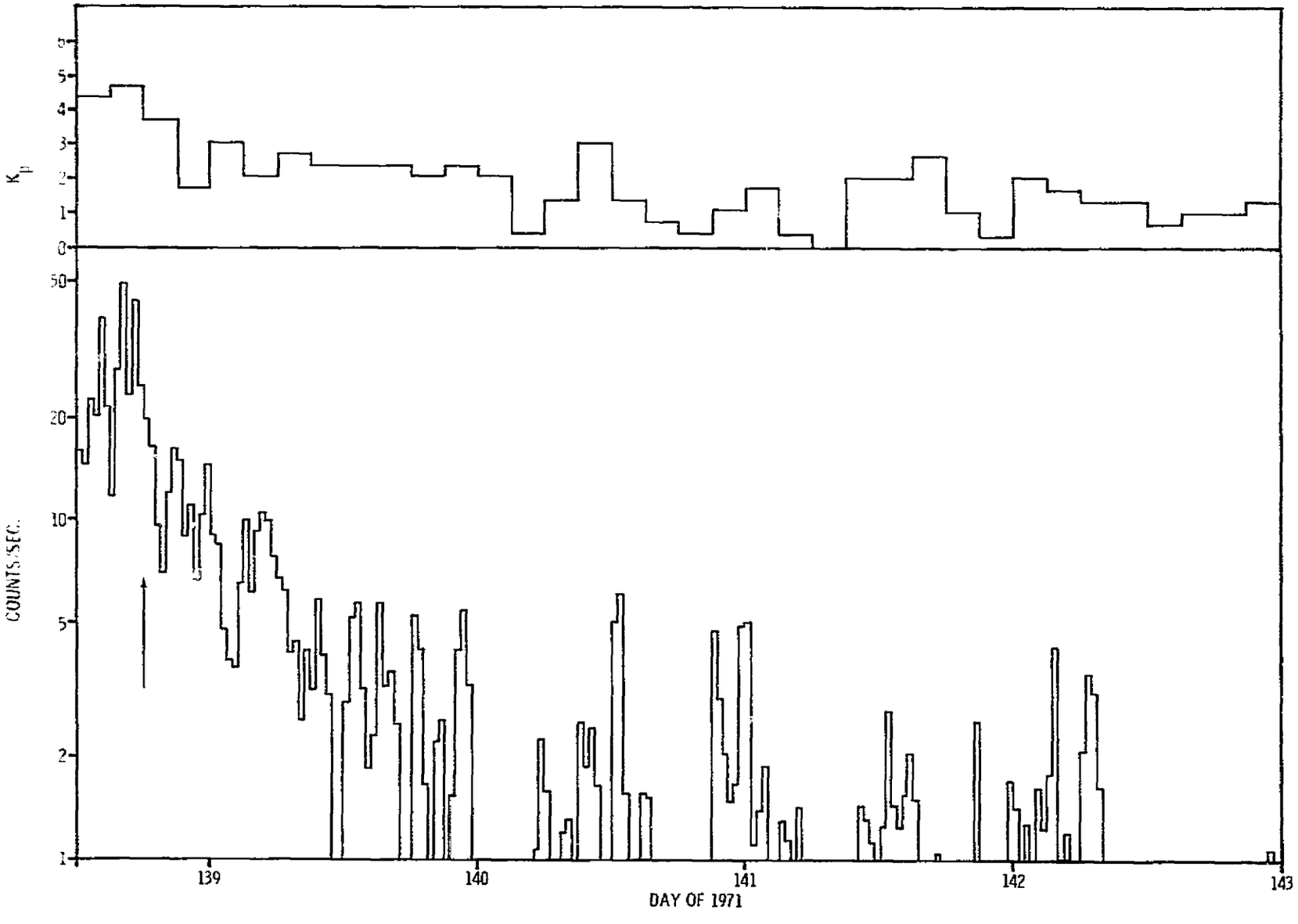
$K_p$
9
5
4
3
2
1
0
50
20
10
5
2
1
COUNTS/SEC.
139
140
141
142
143
DAY OF 1971

crossing, i.e. these fluxes first appear approximately 4 days prior to crossing. These fluxes are distinguished by their greater intensity than either the Type I or Type II events discussed earlier; and, unlike the other two types, they are strongly correlated with Kp. As can be seen from the figure, the fluxes are absent when Kp is below 1+. Although the connection between the geomagnetic activity index Kp and events at the moon far upstream of the earth may not be obvious, Kp has been shown to be an indirect indicator of the velocity of the solar wind (Snyder et al., 1963). Thus these Type III fluxes appear to originate at or near the lunar terminators and are influenced by solar-wind conditions. The occurrence, if any, of thes fluxes at the lunar dayside surface is impossible to determine since they are considerably weaker than the photoelectron fluxes observed at the surface on the sunlit hemisphere (Reasoner and Burke, 1972) and would be masked by the photoelectrons.

It was argued (Reasoner, 1975) that the Type II and Type III events were the result of interactions between the solar wind and the lunar body which served to decouple and/or thermalize electrons out of the solar wind and scatter them to the lunar surface. It was further argued that the TypeIII events, due to their correlation with distance from the terminator and with Kp, were a consequence of an interaction at or near the lunar limb with the solar wind. Parenthetically, it is expected that many of the questions concerning detailed interaction mechanisms could be answered with proper plasma and magnetic field detectors on board the proposed Lunar Polar Orbiter.

## II. Implications of the Lunar Night Flux Events

These lunar night flux events, although weak in magnitude compared to sources such as the direct solar wind, magnetosheath, and plasma sheet, are nonetheless significant in view of the fact that lunar photoelectrons are not available to provide a return current. Consequently, these electrons should be capable of affecting the lunar nightside surface potential. Theoretical calculations of Manka (1973) based on plasma probe theory result in a value of -38 volts for the lunar nightside surface potential when the moon is in the solar wind. Experimental measurements of positive ion fluxes to lunar night surface by the ALSEP/Suprathermal Ion Detector Experiment (SIDE) (Freeman and Ibrahim, 1974) indicate that the lunar nightside potential is actually considerably higher, on the order of a few hundred volts. We suggest therefore that the lunar night electrons flux events, with mean energies in the range of 100-200 volts, are responsible for driving the lunar surface potential to the large negative values inferred by the SIDE measurements. We note that the measured ion densities were in the range 0.05 ions/$cm^3$, which would be of the correct order to provide flux balance to the lunar surface.

## III. Particle Shadowing

Placement of charged particle detectors on the lunar surface by the Apollo/ALSEP program presented many unique problems in data evaluation. We have already referred to the problems associated with contaminating photoelectrons (Reasoner and Burke, 1972) which prevented measurement of the lowest energy portion of the ambient electron spectrum. Another problem, that of particle shadowing, arises because the size of the lunar body is large compared to the scale size of particle cyclotron orbits in the magnetic field, particularly in the case of electrons. For certain orientations of the ambient magnetic field, particles cannot reach the CPLEE analyzers because their spiraling trajectory in the magnetic field carried them into the lunar surface.

As a first step, computations were done assuming a flat, uniform lunar surface with only external magnetic fields. Local remnant magnetic fields and surface electrostatic potentials were neglected. Particle trajectories were computed for various orientations in latitude $\theta$ and longitude $\phi$ of the external magnetic field. In this coordinate system $\theta = 0$ was the lunar equatorial plane and $\phi = 0$ was the direction of local vertical. The results of this computation are shown in Figure 5. The "open zones" for both the A and B analyzers are shown. It is seen that the open zones are roughly circles centered around the analyzer look directions. The analyzer B zone is distorted since the look direction is not symmetrical relative to the surface.

Figure 5

Zones of allowed direction of the external magnetic field for detection of electrons by the CPLEE A and B analyzers.

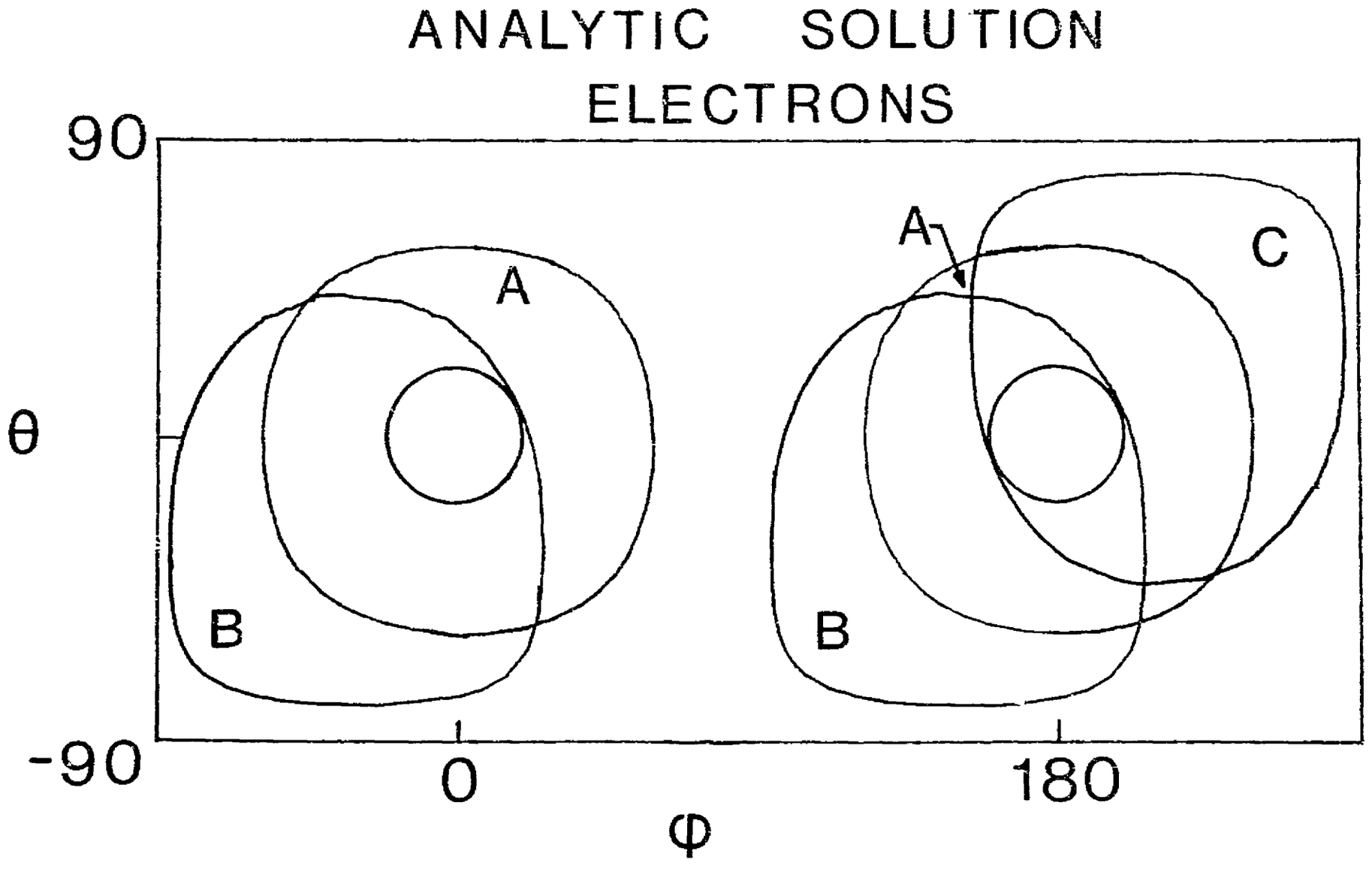
ANALYTIC SOLUTION
ELECTRONS
90
θ
-90
0
180
Φ
A
B
A
C
B

The next step was to include the effects of local remnant magnetic fields. Although there were no magnetometer measurements at the ALSEP site on Apollo 14, Lunar Portable Magnetometer measurements (Dyal et al., 1971) were made at two sites in the vicinity from which an ALSEP site field was computed under the assumption that the remnant field could be represented by a dipole source. The geometry and magnetic field values used in the calculation are shown in Figure 6. The inferred field at the ALSEP site was a 75 $\gamma$ field directed generally downward and to the southeast. Particle trajectories were traced in the combination of a 5 $\gamma$ external field and the inferred local dipolar field to yield the "open zones" in $\theta$ - $\phi$ space shown in Figure 7. Comparing this figure with Figure 5, the distortions can be easily discerned. Also included in the figure are the open zones for a mythical C analyzer which is oriented 60° from local vertical toward lunar east, i.e. a complementary direction to the B analyzer. For the moon immersed in an isotropic plasma, the amount of flux actually reaching the surface will be a function of the external magnetic field direction. For external field directions within the intersection of zones A, B, and C the particle flux reaching the surface should be at a maximum. This fact has indeed been verified in studies of plasma sheet particle fluxes (Reiff, 1975).

These studies of particle trajectory modifications by the local remnant fields have allowed resolution of some puzzling questions concerning the photoelectron layer and the potential distribution near the lunar surface. Theoretical calculations of the expected lunar surface potential in the presence of plasma sheet fluxes by flux balance techniques (c.f. Burke et al., 1975)

Figure 6

Geometry of the Apollo 14 ALSEP site and vicinity showing magnetic field vectors measured by the Lunar Portable Magnetometer and the inferred magnetic field at the ALSEP site under the assumption that the remnant field source could be represented by an equivalent dipole.

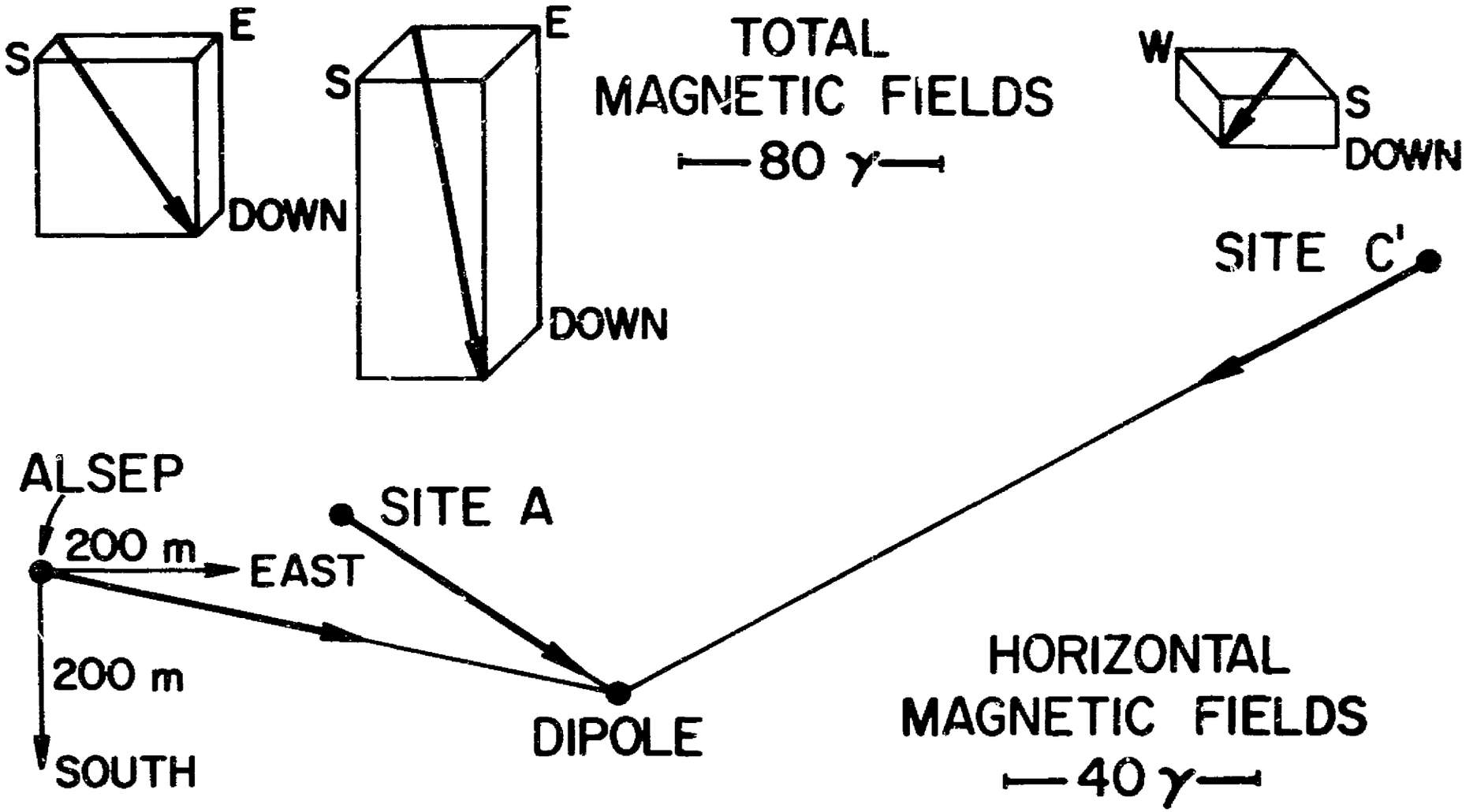
S
E
DOWN
S
E
DOWN
TOTAL
MAGNETIC FIELDS
— 80 γ —
W
S
DOWN
SITE C'
ALSEP
200 m
EAST
SITE A
200 m
SOUTH
DIPOLE
HORIZONTAL
MAGNETIC FIELDS
— 40 γ —

Figure 7

Zones of allowed direction of the external magnetic field with the local remnant field superimposed for detection of electrons by the CPLEE A and B analyzers and a ficticious "C analyzer" oriented 60° from local vertical toward lunar east. Flux access to the lunar surface is maximum when the external field direction lies within the intersection of the three zones.

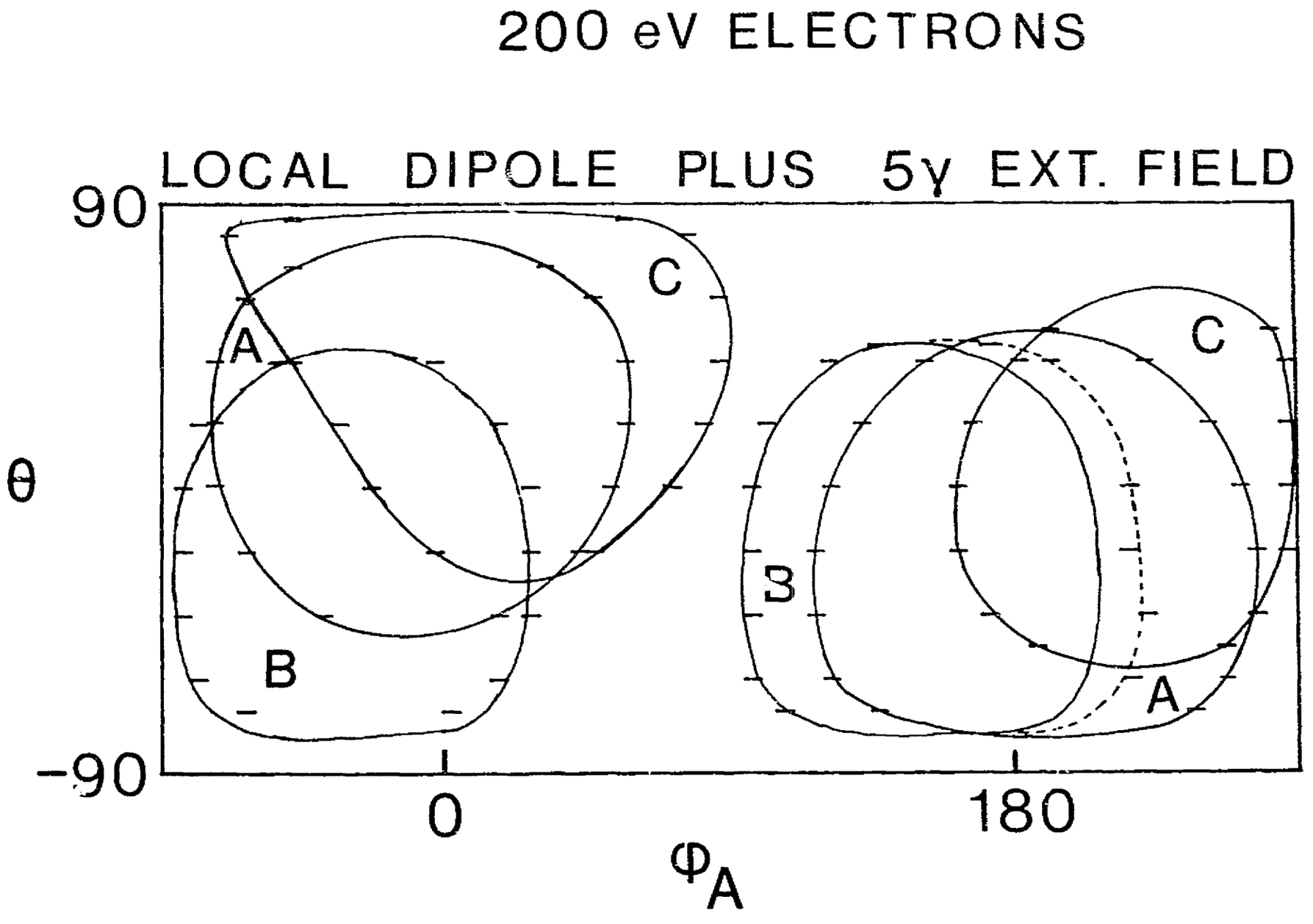
200 eV ELECTRONS
LOCAL DIPOLE PLUS 5γ EXT. FIELD
90
-90
θ
0
180
$\Phi_A$
A
B
C
A
B
C

have usually resulted in a lower value than that actually observed by observing returning photoelectrons. However, the effect of the local remnant magnetic field is to affect the trajectories of incoming electrons much more than those of incoming ions, which leads to the creation of a charge separation electric field. This charge separation field produces an additional potential barrier to escaping photoelectrons and results in an apparent surface potential higher than that given from theoretical flux balance calculations. The situation is depicted schematically in Figure 8. Near the surface the electric field is due mainly to the photoelectron layer with a scale length of only a few meters. The photoelectron layer potential $\phi_{pe}$ is given by the flux balance calculation. However, extending out to ~1 km above the surface (the scale length of the local magnetic field) lies a charge separation potential $\phi_{cs}$ produced by modification of the trajectories of the incoming ions and electrons. A surface-generated photoelectron must then surmount the total barrier $\phi_{pe} + \phi_{cs}$ in order to escape, and without the result outlined here it would be incorrectly concluded from observational data that the potential barrier due to photoelectrons alone was the total barrier height.

Figure 8

A schematic of the electrostatic potential distribution when the sunlit moon is in the plasma sheet. See text for an explanation.

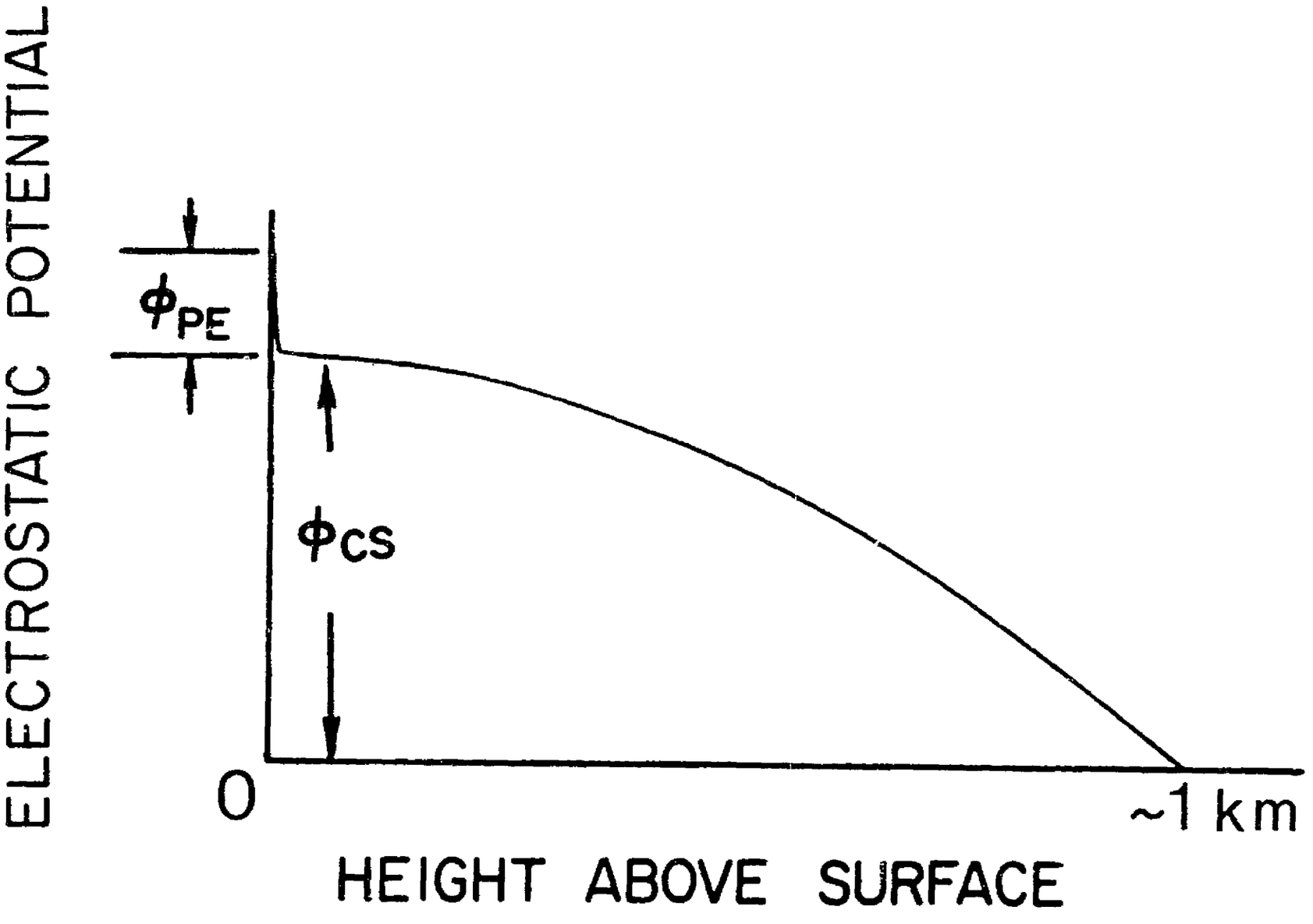
ELECTROSTATIC POTENTIAL
$\phi_{PE}$
$\phi_{CS}$
0
~1 km
HEIGHT ABOVE SURFACE

## Conclusions

The interaction of space plasmas with the moon has indeed been a fascinating area of study, for the moon is unlike any other solar system body whose interactions have been studied *in situ*. The moon possesses no sensible atmosphere or large-scale magnetic field, and hence the interactions are weak though nonetheless interesting.

Charged particles and solar photons have direct access to the lunar surface, and the surface-based charged particle detectors have shown a number of interesting phenomena; for example, electrostatic surface potentials, charge separation potentials caused by particle interactions with local remnant magnetic fields, disturbances of the solar wind at the lunar limb, and modification of the lunar night surface potential by the impact of thermalized solar wind electrons.

Acknowledgements

The principal investigator was on leave-of-absence from Rice University as an NAS/NRC Senior Postdoctoral Fellow at Marshall Space Flight Center from September 1974 to September 1975. I would like to acknowledge the help and cooperation given by Mr. John B. Hanley (deceased) and Dr. Desiree Stuart-Alexander of the Lunar Programs Office for approving this arrangement and for allowing the research effort to continue. I would like to thank Dr. C. R. Chappell and the NAS/NRC program at MSFC for providing time and facilities for me to continue this research effort at MSFC.

Particular compliments should be paid to Dr. William J. Burke and Dr. Patricia Hofer Reiff who continued the research program at Rice University in my absence. Also, Mr. Wayne A. Smith of Rice provided invaluable aid in assuming the management duties of the grant.

## References

Burke, W. J., P. H. Reiff and D. L. Reasoner, "The Effect of Local Magnetic Fields on the Lunar Photoelectron Layer while the Moon is in the Plasma Sheet," Geochem. Cosmochem. Acta, Suppl. 6, p. 2985, 1975

Dyal. P., C. W. Parkin, C. P. Sonnett, R. L. DuBois, and G. Simmons, "Lunar Portable Magnetometer Experiment," Apollo 14 Preliminary Science Report, NASA SP-272, 1971.

Freeman, J. W., Jr., and M. E. Ibrahim, "The Lunar Electric Potential and its Plasma Sheath Effects," abstract, Lunar Interactions, p. 86, Lunar Science Institute, 1974.

Manka, R. H., "Plasma and Potential at the Lunar Surface," in Photon and Particle Interactions with Surfaces in Space, (ed. R. J. L. Grard) p. 347, D. Reidel, 1973.

Reasoner, D. L., "Lunar Nightside Electron Fluxes," Geochem. Cosmochem. Acta, Suppl. 6, Vol. 3, p. 3023, 1975.

Reasoner, D. L. and W. J. Burke, "Characteristics of the Lunar Photoelectron Layer," J. Geophys. Res., 77, 6671, 1972.

Reiff, Patricia H., "Modification of Particle Fluxes at the Lunar Surface by Electric and Magnetic Fields," Ph.D. Thesis, Rice University,April 1975.

Scudder, J. D., D. L. Lind, and K. W. Ogilvie, "Electron Observations in the Solar Wind and Magnetosheath," J. Geophys. Res., 78, 6535, 1973.

Snyder, C. W., M. Neugebauer, and U. R. Rao, "The Solar Wind Velocity and its Correlation with Cosmic Ray Variations and with Solar and Geomagnetic Activity," J. Geophys. Res., 68, 6361, 1963.

# APPENDIX A

## Publications

## Publications

1. Reasoner, D. L., "Observations of Low-Energy Electrons Upstream of the Earth's Bow Shock," J. Geophys. Res., 80, 187, 1975.

2. Reiff, Patricia H. and D. L. Reasoner," The Magnetosheath Electron Population at Lunar Distance: General Features," J. Geophys. Res., 80, 1232, 1975.

3. Reiff, P. H., "Modification of Particle Fluxes at the Lunar Surface by Electric and Magnetic Fields," Ph.D. Thesis, Rice University, Houston, TX, April, 1975.

4. Reasoner, D. L., "Lunar Nightside Electron Fluxes," Geochem. Cosmochem. Acta, Suppl. 6, Proceedings of the Sixth Lunar Science Conference, Vol. 3, p. 3023, 1975.

5. Burke, W. J., P. H. Reiff, and D. L. Reasoner, "The Effect of Local Magnetic Fields on the Lunar Photoelectron Layer while the Moon is in the Plasma Sheet," Geochem. Cosmochem. Acta. Suppl. 6, Proceedings of the Sixth Lunar Science Conference, Vol. 3, p. 2985, 1975.

6. Reiff, P. H., "Magnetic Shadowing of Charged Particles by an Extended Surface," J. Geophys. Res., in press, 1976.

7. Reiff, P. H. and W. J. Burke, "Interactions of the Plasma Sheet with the Lunar Surface at the Apollo 14 Site," J. Geophys. Res., in press, 1976.

# APPENDIX B

## Reprints and Abstracts

"Observations of Low-Energy Electrons Upstream of the Earth's Bow Shock", David L. Reasoner.

"The Magnetosheath Electron Population at Lunar Distance: General Features", Patricia H. Reiff and David L. Reasoner.

"The Effect of Local Magnetic Fields on the Lunar Photoelectron Layer While the Moon Is In the Plasma Sheet", William J. Burke, Patricia H. Reiff, and David L. Reasoner.

"Lunar Nightside Electron Fluxes" by David L. Reasoner.

PRECEDING PAGE BLANK NOT FILMED

# Observations of Low-Energy Electrons Upstream of the Earth's Bow Shock

DAVID L. REASONER[1]

*Department of Space Physics and Astronomy, Rice University, Houston, Texas 77001*

Observations of electron fluxes with a lunar-based electron spectrometer when the moon was upstream of the earth have shown that a subset of observed fluxes are strongly controlled by the interplanetary magnetic field (IMF) direction. The fluxes occur only when the IMF lines connect back to the earth's bow shock. Observed densities and temperatures were in the ranges $2\text{–}4 \times 10^{-3}$ cm$^{-3}$ and $1.7\text{–}2.8 \times 10^{6}$ °K. It is shown that these electrons can account for increases in effective solar wind electron temperatures on bow shock connected field lines, which have been observed previously by other investigators. It is further shown that if a model of the bow shock with an electrostatic potential barrier is assumed, the potential can be estimated to be 500 V.

Observations of charged particles upstream in the solar wind, whose origin was apparently at the bow shock, have been reported by several authors (see, e.g., *Anderson* [1969], *Lin et al.* [1974], and references therein). The common feature of these observations is that there is an interplanetary charged particle component that is strongly controlled by the direction of the interplanetary magnetic field (IMF). The particles were only observed at a particular upstream location when the field line through the observation point intersected the assumed bow shock envelope. In this paper are presented observations of low-energy (40–1000 eV) electrons from a lunar-based instrument during lunar night periods. The instrument was viewing into the downstream solar wind cavity, and the moon was upstream of the bow shock. Sporadic low-energy fluxes were observed throughout lunar night periods, and it is shown that a subset of these electron flux events occur only when there is field line connection to the bow shock.

## Data

The particle measurements were made with the charged particle lunar environment experiment (CPLEE), a component of the Apollo 14 Alsep system. (For an instrument description see *Burke and Reasoner* [1972].) Magnetic field data from the Explorer 35/Ames Research Center magnetometer in lunar orbit provided field line geometry information.

Data from four contiguous lunar night periods in February to May 1971 were examined for the presence of electron fluxes that exhibited control by the IMF direction, in particular for electron fluxes that were present only when the IMF line passing through the moon intersected the earth's bow shock. The bow shock surface was represented by an aberrated hyperboloid of revolution, a model first proposed by *Scudder et al.* [1973]. For a given value of the IMF latitude $\theta$ the equation for the limiting values of the IMF longitude $\phi$ resulted in a quartic in cot $\phi$. This equation in turn was solved for the limiting values of $\phi$ such that the IMF was tangent to the bow shock surface.

Because of gaps in the IMF data it was not possible to categorize all lunar night electron flux events according to the criterion of whether or not the IMF intersected the bow shock. However, when analysis was restricted to only those events where concurrent IMF data were available, it was possible to identify from the data set a total of 10 electron flux events with durations of 30 min or more where the electron flux exhibited strong control by the IMF direction, appearing only when the IMF line connected from the moon downstream to the bow shock. For the sake of brevity we will refer to these events as 'bow shock events' in the remainder of the paper.

An example of a bow shock event is shown in Figure 1. In this figure we display 3-min averages of the counting rate due to 200-eV electrons (lower panel), the IMF longitude $\phi$ (middle panel), and the IMF latitude $\theta$ (upper panel). The limiting values of $\phi$, which, recall, are a function of $\theta$, are shown as dashed lines near ±20°. On this day, May 25, 1971, the solar ecliptic longitude of the moon varied from 4° to 16°, i.e., the moon was almost directly upstream from the bow shock. Two prominent isolated events are seen, one from 0210 to 0230 and the other from 0305 to 0410. Lower-intensity shorter-duration events appear near 0515 and 0620. In all these events are seen the sharp onsets and decays as the value of the IMF longitude $\phi$ passes through the limiting values, a feature quite typical of the total set of these bow shock events.

There are other lower-intensity electron events seen in the figure, but many of these (for example, near 1400) occur at times when either $\theta$ or $\phi$ are at such a value as to preclude intersection of the IMF line with the bow shock. The origin of these fluxes remains unknown, although they may well be associated with local solar wind-lunar interactions. However, the bow shock events are distinguished not only by their dependence upon the IMF direction but also by their greater intensity.

Electron spectra for the longer-duration bow shock events were computed from 30-min averages. These long averages were necessary to gain statistical significance in view of the low counting rates involved. Figure 2 shows the electron spectrum for the period 0315–0345 on May 25, 1971, corresponding to the second large event in Figure 1. In this spectrum and other spectra the data points and standard deviations were computed with the usual statistical techniques. In order to determine densities and temperatures a $\chi^2$ minimization algorithm called Curfit [*Bevington*, 1969] was used to fit both Maxwellians and $\kappa$ functions [*Vasyliunas*, 1968] to the data points. It was found that in most cases the $\kappa$ function, with its power law representation of a high-energy tail, resulted in a better fit (smaller $\chi^2$) than the Maxwellian function did. For example, for the data points of Figure 2, a Maxwellian fit resulted in the parameters $n = 2.9 \times 10^{-3}$, $T = 1.1 \times 10^{6}$ °K, and $\chi^2 = 0.31$, whereas a $\kappa$ function fit resulted in $n = 3.5 \times 10^{-3}$, $T = 2.5 \times 10^{6}$ °K, $\kappa = 3.3$, and $\chi^2 = 0.20$. The dashed line on the figure then represents the fitted $\kappa$ function spectrum. The fitted spectra for the events studied gave densities in the range $2\text{–}4 \times 10^{-3}$ el·cm$^{-3}$ and temperatures (thermal energies) in the range $1.7 \times 10^{6}$ to $2.8 \times 10^{6}$ °K (150–250 eV).

[1] Now at Marshall Space Flight Center, Huntsville, Alabama 35812.

Copyright © 1975 by the American Geophysical Union.

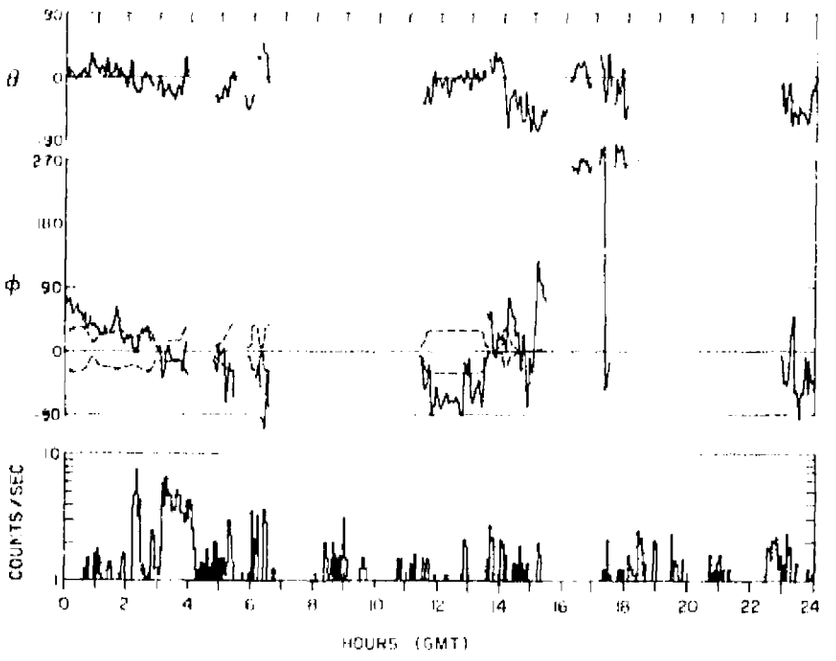


Fig. 1. Low-energy electron and IMF data from May 25, 1971, showing bow shock associated electron events between 0210 and 0230 and again between 0305 and 0410. The dashed lines on the plot of the IMF longitude $\phi$ are the limiting values for bow shock intersection.

## Discussion

*Scudder et al.* [1973] report a study of solar wind electron temperatures with Ogo 5 wherein they separated the data set into two subsets based on whether or not the IMF lines through the observation point intersected the bow shock. They found a slight tendency for the electron temperature to be larger when the field lines intersected the bow shock, although the statistical reliability of the statement was greater than 50% on only one out of five orbits studied (see their Table 1 and Figure 3). They attributed these higher temperatures to a non-Maxwellian electron population with energies of the order of 100 eV. It is therefore suggested that the bow shock associated electron fluxes reported herein are one and the same with the electron fluxes responsible for the temperature increases reported by *Scudder et al.* [1973].

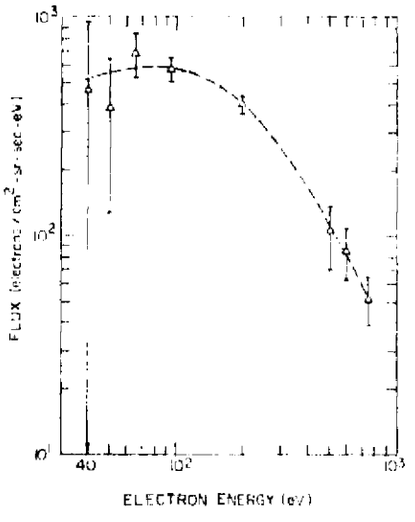


Fig. 2. The electron energy spectrum for the period 0315–0345 on May 25, 1971, corresponding to the second large flux enhancement in Figure 1. The dashed line is a $\kappa$ function fit to the data points resulting in the parameters $n = 3.5 \times 10^{-3}$, $T_e = 2.5 \times 10^6$ °K, and $\kappa = 3.3$.

To emphasize this last point, in Figure 3 we have plotted a superposition of a typical solar wind electron energy spectrum as reported by *Montgomery et al.* [1970] with $n = 5.5$ cm$^{-3}$ and $T_e = 1.6 \times 10^5$ °K and the spectrum fitted to the data of Figure 2. The bow shock electrons appear essentially as a small high-energy tail upon the main spectrum. This high-energy tail would result in a higher temperature from a moment calculation, although its true nature would be effectively masked. However, for this study the moon acted to shield the instrument from the solar wind electrons and allowed an uncontaminated measure of the properties of these bow shock electrons.

It can easily be shown that the effective temperature of the sum of two distributions $f_1(v)$ and $f_2(v)$, where $n_1 \gg n_2$ and $T_1 > T_2$, can be approximated by $T_{eff} = T_1 + (n_2 T_2 / n_1)$. Performing the calculation for the data shown above gives $T_{eff} = 1.62 \times 10^5$ versus $T_1 = 1.60 \times 10^5$. This small increase in effective temperature is of the same order of magnitude as that reported by *Scudder et al.* [1973] in their study.

Bow shock observations by *Fredricks et al.* [1970] indicate that the shock may be classed as turbulent, that is, ion electrostatic waves play an important role in randomizing the incoming ion stream into postshock conditions. Yet it must be kept in mind that the shock does not act as an impenetrable wall between the preshock plasma and the postshock plasma. Rather, there is interpenetration of ions from each region into the other, and in the shock transition itself the ion distribution becomes bimodal. This can lead to growth of wave modes that act in a self-consistent manner to convert the cool preshock ion distribution into the hot postshock distribution. This intermixing of distribution functions was originally discussed by *Mott-Smith* [1951] in connection with classical gas shocks, and a discussion applicable to collisionless plasma

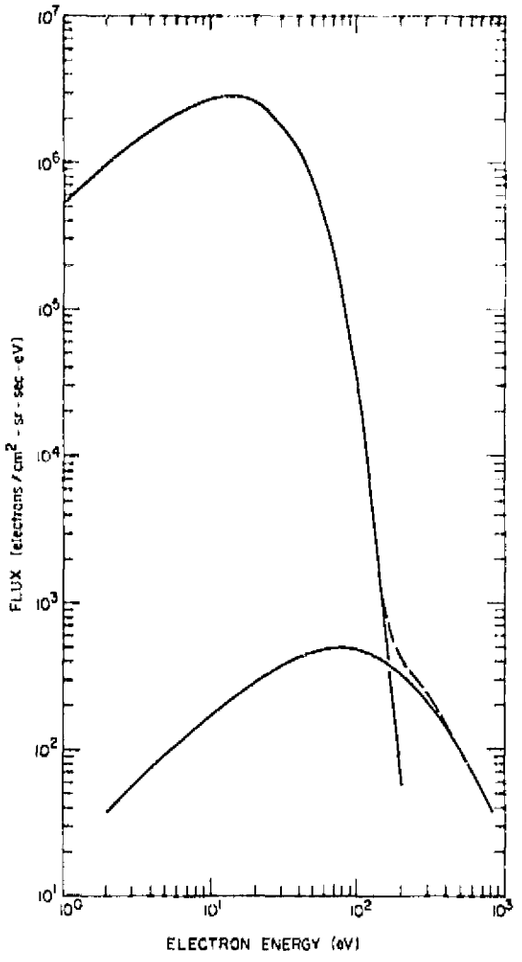


Fig. 3. A superposition of a typical solar wind electron spectrum from *Montgomery et al.* [1970] and the electron spectrum of Figure 2. This shows that these bow shock electrons result in a small increase in the effective solar wind electron temperature. The dashed line is the sum of the two spectra.

shocks can be found in the paper by *Tidman and Krall* [1971]. The upstream component of the downstream ion distribution has been observed experimentally by *Montgomery et al.* [1970].

By contrast the electron distribution does not become bimodal in the shock transition, and hence the conditions are not immediately available for electron electrostatic wave growth. It is an observational fact that solar wind electrons are quite different in character from magnetosheath electrons [e.g., *Montgomery et al.*, 1970], and therefore there must exist a mechanism that prevents complete mixing of the preshock and postshock electron distributions.

*Montgomery and Joyce* [1969] have developed a model of a laminar electrostatic shock that provides such a mechanism. In their model the ions on both sides of the shock were at zero temperature (this assumption thus disposing of the need for an additional dissipation mechanism), whereas the postshock electrons were treated as a sum of free and trapped distributions. An estimate of the potential drop across the shock can be obtained by using the measured electron spectrum (Figure 2) and a typical magnetosheath distribution [*Montgomery et al.*, 1970] and by assuming that the Liouville theorem applies. From the electron spectrum of Figure 2, $f_0(v = 0) = 3.9 \times 10^{-30}$ cm$^{-6}$ s$^3$. This value occurs on the magnetosheath distribution at a velocity of $1.35 \times 10^9$ cm/s, corresponding to a total potential drop of 500 V. Because the measured density at $X_{GSE} \simeq 60\ R_E$ may well be lower than that near the bow shock, the value of 500 V is an upper limit.

The above arguments have necessarily been ad hoc and by no means are offered as proof that such an electrostatic potential barrier actually exists. The required electron distribution separation mechanism could well be provided by other wave-related means. However, *Neugebauer* [1970] reported a decrease in the solar wind ion flow energy without an increase in temperature just ahead of the bow shock and postulated that an electrostatic potential drop with a maximum value of 200 V was responsible. It may well be then that if a potential drop across the shock exists, it is not confined entirely to the shock transition layer but rather is distributed also upstream and downstream of the shock.

## Summary

Low-energy electrons have been observed at lunar orbit upstream of the bow shock that displayed the following characteristics: (1) The electrons were controlled by the IMF direction, appearing only when the IMF line through the observation point connected back to the bow shock. (2) Densities were in the range 2–4 $\times$ 10$^{-3}$, and temperatures (mean energies) were in the range 1.7–2.8 $\times$ 10$^6$ °K (150–250 eV).

The electrons were shown to be able to account for the small increases in solar wind electron temperatures on bow shock connected field lines observed by *Scudder et al.* [1973]. If it is assumed that these electrons are the high-energy tail of the magnetosheath electron distribution leaking back upstream through an electrostatic potential barrier, then a total potential drop of 500 V is estimated. This complements an earlier observation of *Neugebauer* [1970] indicating a 200-V drop in a layer immediately ahead of the bow shock. It is therefore suggested that an electrostatic potential drop that acts to prevent the majority of the downstream electron distribution from mixing with the upstream plasma deserves serious consideration in theories and models of the earth's bow shock.

*Acknowledgments.* The author is indebted to D. S. Colburn of the Ames Research Center for making Explorer 35 magnetometer data available. This research was supported by National Aeronautics and Space Administration grant NSG-07025. The author is presently a NAS NRC senior postdoctoral fellow at Marshall Space Flight Center.

The Editor thanks R. P. Lin for his assistance in evaluating this report.

## References

Anderson, K. A., Energetic electrons of terrestrial origin behind the bow shock and upstream in the solar wind, *J. Geophys. Res.*, *74*, 95, 1969.

Bevington, P. R., *Data Reduction and Error Analysis for the Physical Sciences*, chap. 11, McGraw-Hill, New York, 9.

Burke, W. J., and D. L. Reasoner, Absence of the plasma sheet at lunar distance during geomagnetic quiet times, *Planet. Space Sci.*, *20*, 424, 1972.

Fredricks, R. W., G. M. Crook, C. F. Kennel, I. M. Green, F. L. Scarf, P. J. Coleman, and C. T. Russell, Ogo 5 observations of electrostatic turbulence in bow shock magnetic structures, *J. Geophys. Res.*, *75*, 3751, 1970.

Lin, R. P., C.-I. Meng, and K. A. Anderson, 30- to 100-keV protons upstream from the earth's bow shock, *J. Geophys. Res.*, *79*, 489, 1974.

Montgomery, D., and G. Joyce, Shock-like solutions of the electrostatic Vlasov equation, *J. Plasma Phys.*, *3*(1), 1, 1969.

Montgomery, M. D., J. R. Asbridge, and S. J. Bame, Vela 4 plasma observations near the earth's bow shock, *J. Geophys. Res.*, *75*, 1217, 1970.

Mott-Smith, H., The solution of the Boltzmann equation for a shock wave, *Phys. Rev., 82*, 885, 1951.
Neugebauer, M., Initial deceleration of solar wind positive ions in the earth's bow shock, *J. Geophys. Res., 75*, 717, 1970.
Scudder, J. D., D. L. Lind, and K. W. Ogilvie, Electron observations in the solar wind and magnetosheath, *J. Geophys. Res., 78*, 6535, 1973.
Tidman, D. A., and N. A. Krall, *Shock Waves in Collisionless Plasmas*, chap. 8, Interscience, New York, 1971.
Vasyliunas, V. M., A survey of low-energy electrons in the evening sector of the magnetosphere with Ogo 1 and Ogo 3, *J. Geophys. Res., 73*, 2839, 1968.

(Received August 19, 1974;
accepted September 25, 1974.)

# The Magnetosheath Electron Population at Lunar Distance: General Features

PATRICIA H. REIFF AND DAVID L. REASONER

*Department of Space Physics and Astronomy, Rice University, Houston, Texas 77001*

The spatial extent and energy distribution function of the magnetosheath electron population at lunar distance have been analyzed by using measurements from the Apollo 14 charged particle lunar environment experiment (CPLEE). The magnetotail is shown to be approximately 52 $R_E$ in diameter. The mean bow shock surface has a cross section of about 91 $R_E$. The average aberration angle measured is about 3°. The electron distribution function reveals two distinct particle populations. The first, at low energies (40 eV $< E <$ 200 eV), is well characterized by a nearly isotropic Maxwellian distribution, with temperatures in the range 15–25 eV. Densities calculated from fitted functions range from 4–8 $cm^{-3}$ at the bow shock to 1–2 $cm^{-3}$ near the magnetopause. The high-energy portion of the spectrum (200 eV $< E <$ 2000 eV), however, is generally anisotropic and is generally denser and more energetic in the dawn magnetosheath than in the dusk magnetosheath. Separate Maxwellian fits to the high-energy population yield densities near 0.02 (0.10) $cm^{-3}$ and temperatures near 200 (250) eV for the dusk (dawn) magnetosheath. It is argued that these particles originate at the bow shock rather than in the plasma sheet.

The general characteristics of the magnetosheath electron population have been reported for the near-earth regions [e.g., *Scudder et al.*, 1973] and the polar cusps [*Winningham*, 1972]. The lunar distant magnetosheath ion population has been extensively studied, both from lunar surface observations [*Fenner*, 1971, 1974] and from the Explorer 33 and 35 satellites [*Howe*, 1971; *Howe and Binsack*, 1972].

The magnetosheath electron population at lunar distance has been largely unexamined. *Howe* [1971] included electron data from Faraday cups on Explorer 33 and 35; generally, however, only one energy range was above background current, allowing only limited spectral information. *Goldstein* [1974] presented one lunation of electron density and temperature; however, his study was primarily concerned with photoelectron sheath properties.

In the present study, four inbound (dusk) and three outbound (dawn) magnetosheath passages were examined with the charged particle lunar environment experiment (CPLEE). Average boundary locations computed from the complete data set are consistent with the predictions of fluid dynamics. Electron characteristics for the two least disturbed passages are presented here in detail. Energy spectra show an unexpected high-energy tail superimposed on the expected low-energy magnetosheath distribution. The high-energy tail is most pronounced on the dawn side and appears to be generated at the bow shock.

## EXPERIMENT

The CPLEE instrument is a lunar-based ion-electron spectrometer, measuring particle fluxes in the energy range 40 eV to 20 keV. A description of the instrument and deployment is given by *Reasoner and O'Brien* [1972]; therefore only a few pertinent features will be repeated here. The instrument contains two charged particle analyzers, one whose look direction is local vertical (analyzer A) and one whose look direction is 60° to the west of local vertical (analyzer B). The look directions relative to magnetosheath geometry are shown in Figure 1. The flare of the magnetosheath boundaries is such that the analyzers maintain a nearly constant angle to the expected laminar magnetosheath flow direction (40° and 100° for A and B, respectively, in the dusk sheath; 5° and 55° in the dawn sheath).

## BOUNDARY LOCATIONS: CRITERIA AND RESULTS

In order to establish average boundary locations for the magnetosheath we need a consistent set of criteria to distinguish boundary crossings from random fluctuations in particle fluxes and from interplanetary events. The criteria used here for a bow shock crossing from preshock to postshock conditions are the following: (1) The flux in the lowest-energy channels should abruptly rise, indicating a jump in density. (2) The flux in the medium- to high-energy channels should jump by a factor larger than that in the lowest-energy channels, indicating a coincident jump in mean thermal energy and not just a random increase in density. (3) For events satisfying (1) and (2) but occurring more than 15° in longitude away from the mean bow shock location [*Howe and Binsack*, 1972], Imp 6 interplanetary solar wind data were examined to rule out the possibility of interplanetary shocks.

Figure 2 illustrates several bow shock crossings selected according to these criteria. The top trace presents differential flux for the lowest-energy channel (center energy 40 eV) versus time. The lower trace is a similar plot for a medium-energy channel (94 eV). The arrowheads point to shock crossing times at about 1628, 1703, 1710, 1725, 1835, and 1842 UT, April 5, 1971. The bars beneath indicate sheath periods, the remainder of the time the moon was in the solar wind. The data are unaveraged; i.e., each data point is one CPLEE cycle (19 s). The figure therefore indicates both the sharpness of the transitions (of the order of one cycle) and the magnitude of typical fluctuations in the magnetosheath. Differential flux spectra from just before and just after the 1703 crossing are shown in Figures 5*a* and 5*b* and discussed in a following section.

When the moon crosses the magnetopause from the magnetosheath, it can enter either the high-latitude tail, the plasma sheet, or the boundary layer. These regions differ widely in their particle populations. However, in both the high-latitude tail and the plasma sheet the fluxes at low energies (40–100 eV) are dominated by lunar surface photoelectrons [*Burke and Reasoner*, 1972; *Rich et al.*, 1973]. The boundary layer, discussed by *Akasofu et al.* [1973] near the earth and by *Fenner* [1974], *Hardy et al.* [1974], and *Moore et al.* [1974] at

Copyright © 1975 by the American Geophysical Union.



PRECEDING PAGE BLANK NOT FILMED

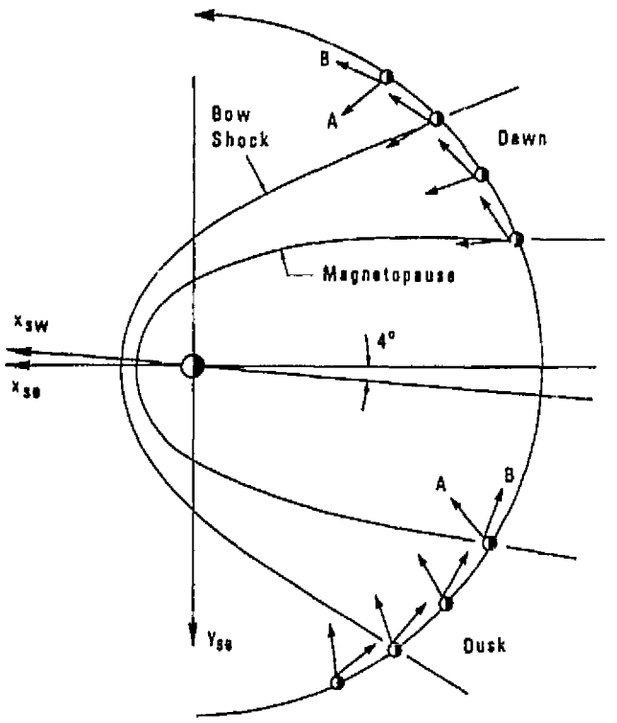


Fig. 1. Ecliptic plane projection of the orbit of the moon, showing the look directions of the two analyzers. The axis of symmetry of the figure is the 'solar wind' $X$ axis, rotated 4° from the earth-sun line.

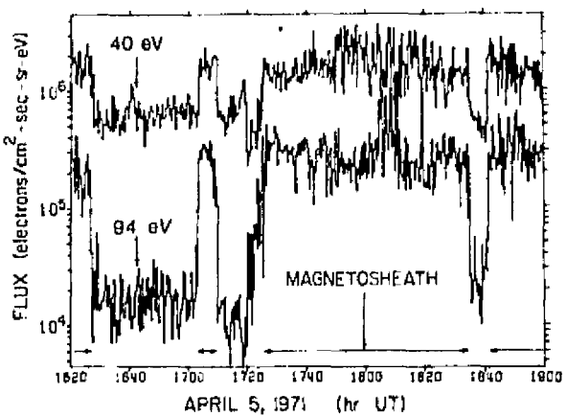


Fig. 2. Unaveraged differential flux versus time for the channels of analyzer A with peak sensitivity at 40 eV (38–43 eV) and 94 eV (86–110 eV). Several bow shock crossings are shown, indicated by the arrowheads.

lunar distance, is readily distinguished by CPLEE proton data or by Explorer 35 magnetic field data. Therefore the criterion for magnetopause crossings is either a transition at low energies to the photoelectron spectrum reported by *Reasoner and Burke* [1972] or a transition to boundary layer conditions.

Within the standard deviations of the measurements the average boundary locations observed by CPLEE are in good agreement with the observations of *Howe and Binsack* [1972]. Table 1 shows a monthly listing of the number of crossings observed and median crossing longitude in solar ecliptic coordinates. Although portions of five lunar orbits are included in the table, only the entries without an asterisk or a dagger are included in the averages. The entry with an asterisk indicates the instrument turned on past the mean boundary, and the entries with a dagger refer to periods in which the instrument was in standby mode during all or part of the time in which boundary crossings were expected. The remaining crossings were used to compute the means and standard deviations shown in the table. The longitude of symmetry of the mean bow shock surface is 176.3° ± 3.2°. The longitude of symmetry of the mean magnetopause is 177.0° ± 3.7°. Within the standard deviations, therefore, the symmetry axes are coincident and are consistent with an average solar wind aberration angle of 3–4°. The average longitudes imply a magnetotail diameter of 52 $R_E$ and a bow shock cross section of 91 $R_E$.

## Magnetosheath Electron Plasma Parameters

We now turn to an examination of the plasma characteristics of the magnetosheath electron population. In this section are presented overviews of a complete dusk (inbound) and dawn (outbound) sheath passage. In the following section we show differential flux spectra from selected times in the two passages and discuss the distribution function in detail. The April 1971 dusk passage and the February 1971 dawn passage were chosen because of the steadiness of the solar wind both in density and in velocity and because of the lack of extreme geomagnetic activity, as evidenced by low $Kp$.

Figures 3 and 4 present numerically integrated pressure and density for the dusk and dawn sheath passages, respectively. The top trace in each figure is computed average energy per particle, i.e., the energy density moment divided by the density moment of the observed distribution function. The middle and

TABLE 1. Boundary Crossing Longitudes ($SE$)

| Month, 1971 | Dusk Bow Shock: Number of Crossings | Dusk Bow Shock: MCL ($\mu$ = 127.2, $\sigma$ = 3.9), deg | Dusk Magnetopause: Number of Crossings | Dusk Magnetopause: MCL ($\mu$ = 151.4, $\sigma$ = 4.4), deg | Dawn Magnetopause: Number of Crossings | Dawn Magnetopause: MCL ($\mu$ = 202.5, $\sigma$ = 3.0), deg | Dawn Bow Shock: Number of Crossings | Dawn Bow Shock: MCL ($\mu$ = 225.3, $\sigma$ = 2.6), deg |
|---|---|---|---|---|---|---|---|---|
| Feb. | 3* | 142.95 | 11 | 153.18 | 9 | 201.30 | 5 | 223.75 |
| March | 17 | 122.44 | 21 | 154.33 | 15 | 201.58 | 9 | 226.79 |
| April | 15 | 126.21 | 27 | 152.17 | † | | † | |
| May | 11 | 130.99 | 11 | 150.25 | 17 | 202.85 | 11 | 225.45 |
| June | 17 | 131.22 | 1† | 150.17 | | | | |

MCL stands for median crossing longitude.
* Not included in averages because CPLEE turned on past mean boundary.
† Not included in averages because CPLEE was in standby mode during all or part of boundary crossing.

lower traces indicate the pressure and density, respectively. All parameters are calculated over the energy range 40–2000 eV. Isotropy is assumed and the flow velocity neglected. Since the peak of the distribution function generally lies at or just below the lower energy limit of CPLEE, it is typical that the numerically integrated density is significantly smaller than the actual density. This effect is most pronounced in regions where the plasma is cool, e.g., the solar wind. Comparison with densities calculated from fitted distribution functions indicates an error of 30–80% in the solar wind and ≤30% in the magnetosheath.

Figure 3 begins in the solar wind, with numerically integrated densities near 1 cm$^{-3}$ and pressures near 15 eV cm$^{-3}$, implying average energies near 22 eV. Correcting the density upward by 50% implies average energies closer to 15 eV. Several bow shock crossings are seen from about 1600 UT, April 5, to 0000 UT, April 6. These crossings are readily identifiable by the jump of about a factor of 3 in numerically integrated density and a jump of about 4 in pressure. In the near-shock magnetosheath region the density is fairly stable at 5–6 cm$^{-3}$. The pressure ranges from 80 to 100 eV cm$^{-3}$. The average energy is stable at 27–30 eV. As the moon progresses through the sheath, variations in density and pressure are seen with various magnitudes and time constants, but in general the trend is to lower and lower densities. The average energy, however, is remarkably constant.

The large-magnitude density variations from 0900 to 1900, April 6, are not bow shock crossings, judging from the gradual nature of the transitions and the constancy of the average energy. Instead they are probably due to large-scale longitudinal motion of the magnetosheath. The density minimum at 1040 is, for example, comparable to the density observed 14 hours later, around 0300, April 7. The period of roughly 90 min implies a minimum flapping velocity of 5 km/s, which is certainly not excessive for tail motion [*Bowling and Wolf*, 1974].

Near the magnetopause the density has fallen to nearly its solar wind value (around 0.8 cm$^{-3}$); however, the mean energy is still well above its solar wind value, after the latter has been corrected by 50%. Several magnetopause crossings are shown in Figure 3 from about 2100, April 7, to 0000, April 8, and again at the end of the graph. The low density and low pressure indicate entry into the high-latitude tail.

Figure 4 is a similar trace for a dawn magnetosheath crossing, and similar effects are apparent. The moon begins in the high-latitude tail and undergoes several brief transitions among the plasma sheet, boundary layer, and high-latitude tail before crossing the magnetopause at 0730, February 12, 1971. As was observed in the dusk sheath, the density is a minimum (near 1 cm$^{-3}$) at the magnetopause and rises to a maximum at the bow shock. Several bow shock crossings are seen at about 0200, 0500, and 1100, February 14. These crossings are most easily seen as a decrease in the average energy per particle (the density jump is somewhat obscured by a temporal increase in the incident solar wind density). Two differences are notable from the dusk passage: first, the average energy per particle is more variable in the dawn sheath than in the dusk sheath, and second, the average energy per particle is greater on the dawn side. Both of these effects can be shown to be due to the extremely hot and variable high-energy tail that is observed in the dawn sheath.

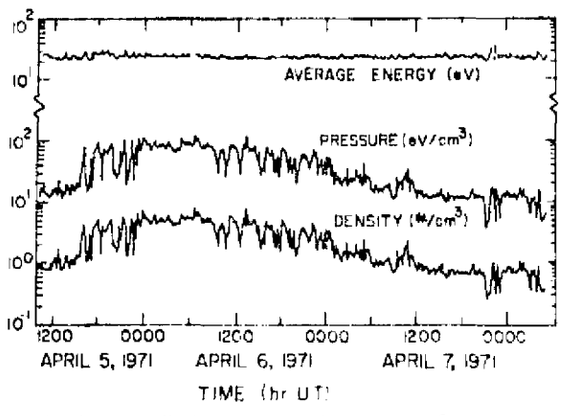


Fig. 3. Numerically integrated 6-min averages of average energy per particle, pressure, and density for a dusk magnetosheath passage. The A analyzer was used, and isotropy was assumed.

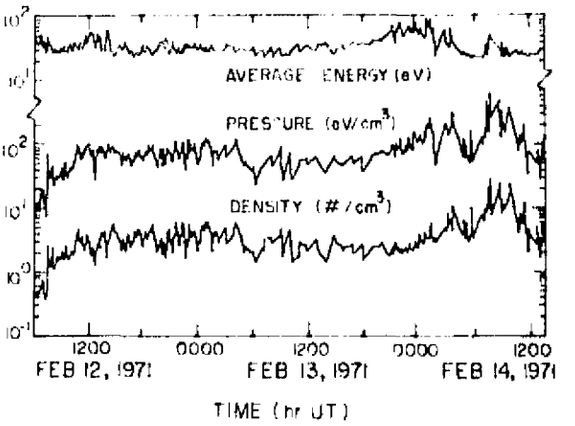


Fig. 4. Same as Figure 3, but data are for a dawn magnetosheath passage.

## MAGNETOSHEATH ELECTRON SPECTRAL CHARACTERISTICS

We present several differential flux spectra in order to study the electron distribution function for the various regions in detail. Figure 5*a* shows a spectrum in the dusk magnetosheath just past a bow shock crossing. We note the appearance of enhanced fluxes above 200 eV, well above the near-background values for these higher-energy channels in the solar wind (cf. Figure 5*b*). As will be seen later, this high-energy excess is a persistent feature of the magnetosheath electron distribution function, although it varies both in absolute magnitude and in relative contribution to the energy density of the entire population. Since the strength of this high-energy tail prohibits a valid Maxwellian fit to the entire spectrum, we choose to quantify the distribution function by dividing the spectrum into two segments: 40–200 eV (which we shall call 'low-energy'), and 200–2000 eV ('high-energy'). This splitting procedure is successful in the dusk sheath and indeed necessary in the dawn sheath, where the high-energy tail often has a different anisotropy ratio than the low-energy portion or else is too strong to allow more conventional functional handling, as, for example, with the $\kappa$ function [*Vasyliunas*, 1968; *Formisano et al.*, 1973]. Therefore we shall attempt a separate Maxwellian distribution function fit for the high-energy portion whenever possible, i.e., if at least the first four high-energy channels are well above background levels.

For these data (Figure 5*a*), all four distribution function fits converged (with reduced $\chi$ square less than 0.8), yielding low-

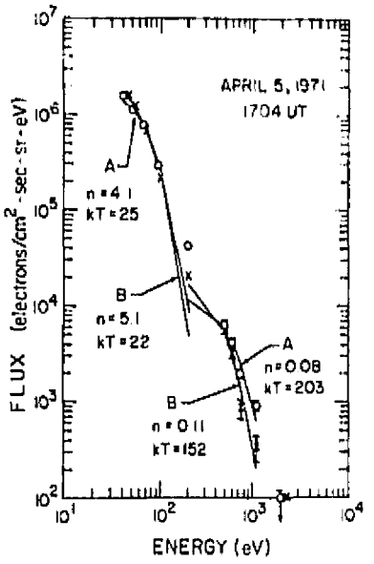


Fig. 5a. Differential flux spectra from the dusk magnetosheath just after a bow shock crossing. The A analyzer data are indicated by circles and the B analyzer data by crosses. The solid lines indicate the flux calculated from the best-fit Maxwellian distribution functions. The density calculated from the Maxwellian distribution function fit is indicated by $n$ (in units of electrons per cubic centimeter), and the temperature is indicated by $kT$ (in units of electron volts).

energy densities of 4.1 (5.1) $cm^{-3}$ and temperatures of 25 (22) eV for the A (B) analyzer. The high-energy portion converged to densities of 0.08 (0.11) $cm^{-3}$ and temperatures of 203 (152) eV for the A (B) analyzer. We notice that in this case, the higher-energy electrons contribute about 14% of the observed energy density.

A typical mid-magnetosheath spectrum from the dusk side is shown in Figure 6. The low-energy population is quite isotropic with a density of 3.8 $cm^{-3}$ and a temperature of 20 eV. The high-energy portion has a density of 0.018 $cm^{-3}$ for the A analyzer and 0.012 $cm^{-3}$ for the B analyzer, both with

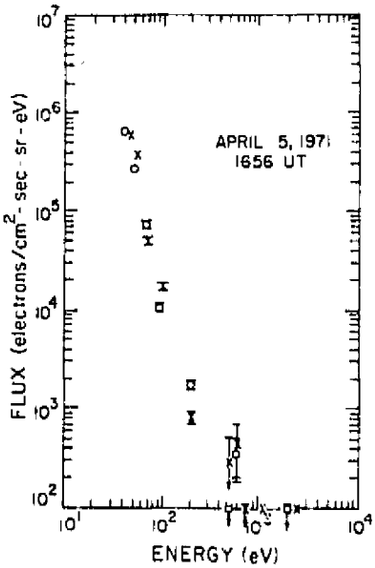


Fig. 5b. Differential flux spectra from the solar wind just prior to a bow shock crossing.

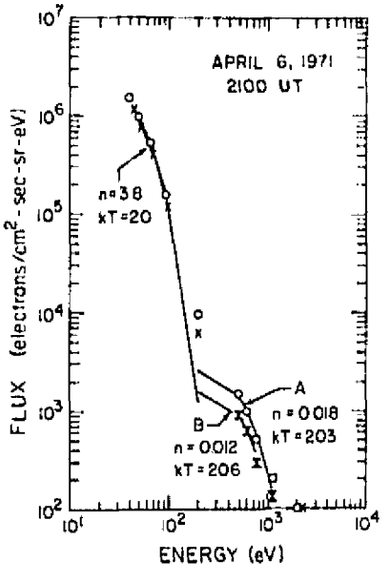


Fig. 6. Typical differential flux spectra from midway through the dusk magnetosheath.

temperatures near 205 eV. Here the high-energy electrons contribute 5% (3%) of the energy density for the A (B) analyzer. The average energy per particle remains at 30 eV.

A spectrum from near the magnetopause (not shown here) reveals a low-energy portion much decreased in density (to around 1 $cm^{-3}$) and temperature (to 16 eV). However, the high-energy portion has remained at nearly the same level (density of around 0.02 $cm^{-3}$ and temperature near 200 eV), thus increasing its proportional contribution to the energy density to nearly 20% and maintaining the average energy per particle at near 30 eV.

Through the dusk sheath we have observed the contribution of the high-energy portion to the total energy density to vary from as little as 1% to as much as 25%. Yet the average energy per particle has remained in the range 27–30 eV. Thus we are led to a remarkable conclusion: the high-energy and low-energy portions of the spectrum grow at the expense of one another. This effect is especially apparent during periods of intense geomagnetic activity, when the high-energy tail all but disappears, leaving an unusually hot low-energy spectrum.

The next series of spectra are from selected periods in the dawn magnetosheath passage. Figure 7 is taken from just outside the dawn magnetopause. As was observed in the dusk side, we see a low-density, cool low-energy spectrum; however, the high-energy portion is extremely dense (0.35 $cm^{-3}$ for the A analyzer and 0.04 $cm^{-3}$ for the B analyzer) and more energetic than the dusk side. Here the high-energy portion contributes 78% of the energy density observed by the A analyzer and 26% for the B analyzer.

A typical spectrum from midway through the dawn sheath is shown in Figure 8. We see that in comparison with Figure 7 the low-energy portion has become denser and warmer (2.4 versus 1.5 $cm^{-3}$ and 22 versus 18 eV), whereas the high-energy portion has become less intense (but not significantly cooler). Thus the average energy per particle, although it is not nearly so stable as that in the dusk sheath, remains the most stable of the observed parameters.

A spectrum from near the dawn bow shock is shown in Figure 9. The low-energy flux in B is greater than the flux in A,

since the look direction of analyzer B is closer to the expected magnetosheath flow direction. The high-energy portion, however, has the opposite sense: the flux in A is greater than the flux in B. Thus, overall, the pressure difference between the A and the B analyzers is only 11%, compared with the 44% implied by the low-energy portion alone.

## Summary of Results

The magnetosheath is highly time variable both in its boundary locations and in the shape and amplitude of its particle distribution function. At lunar distance the boundaries can flap with amplitudes of greater than 10° in longitude [*Burke et al.*, 1973]. The mean boundaries, however, follow approximately the locations one would expect on the basis of extrapolations from observations at distances nearer the earth. The axes of symmetry of both boundaries are aligned with the aberrated solar wind flow direction.

The overviews present a magnetosheath that is well organized at lunar distance. Although magnetosheath model calculations [e.g., *Spreiter and Alksne*, 1969] did not extend back to lunar distance, one expects monotonically decreasing density from bow shock to magnetopause. Our data are consistent with this expectation and in agreement with proton observations at lunar distance [*Fenner*, 1974; *Howe*, 1971]. The unexpected result is the remarkable constancy of the average energy per particle, whereas monotonic cooling from bow shock to magnetopause is predicted from theory.

The individual magnetosheath spectra reveal a highly variable two-component plasma. The two components are distinct but not completely independent; i.e., changes in one part of the spectrum are at least partially compensated by changes in the other part of the spectrum. The high-energy portion is in general denser and more energetic in the dawn sheath than in the dusk sheath. The average energy per particle is more stable in the dusk sheath than in the dawn sheath, but in both cases it is more stable than either the density or the pressure.

## Discussion

The electron distribution function in the magnetosheath is non-Maxwellian, as is well established at locations far closer to the earth. However, this is the first observation of a magnetosheath electron population similar to that of the neighboring plasma sheet. We argue that the high-energy magnetosheath electron population originates at the bow shock rather than from the plasma sheet for the following reasons:

First, the density of these particles that we observe in the dawn magnetosheath is comparable to and often substantially greater (up to 1 cm$^{-3}$) than the density observed in the plasma sheet, which generally ranges from 0.05–0.20 cm$^{-3}$ [*Rich et al.*, 1973].

Second, the high-energy density is larger near the bow shock than throughout the rest of the sheath passage.

Third, the virtual appearance and disappearance of these particles at the bow shock suggest bow shock energization and containment. A contributing factor in the process may be a

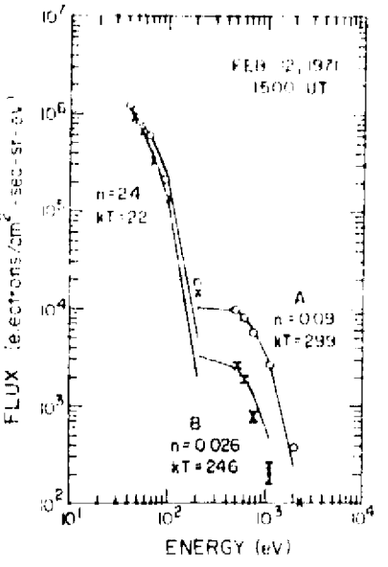


Fig. 8. Typical differential flux spectra from midway through the dawn magnetosheath

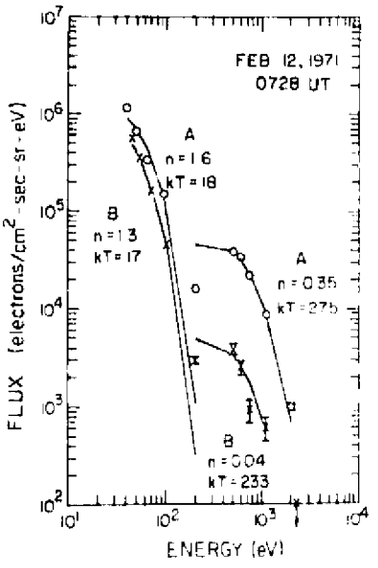


Fig. 7. Dawn magnetosheath differential flux spectra, measured just outside the magnetopause.

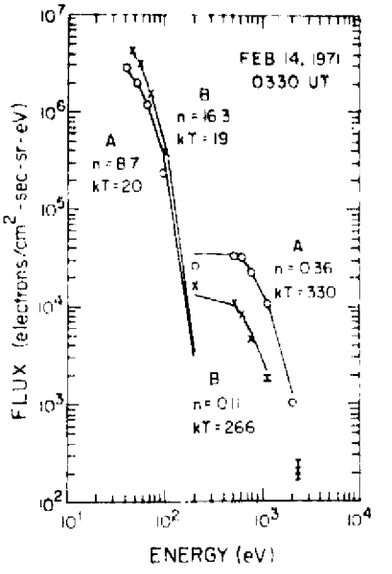


Fig. 9. Differential flux spectra from the dawn magnetosheath adjacent to the bow shock.

potential difference across the bow shock. A potential rise across the bow shock, on the assumption that there is no magnetic field (or magnetic field parallel to the shock normal), would compress and slow incoming protons and would accelerate incoming electrons. A model for an electrostatic shock with postshock trapped electrons is discussed by *Montgomery and Joyce* [1969]. For a magnetic field perpendicular to the shock normal, however, electrons would $\mathbf{E} \times \mathbf{B}$ drift into a region of higher B and be betatron heated. As the 'garden hose' interplanetary magnetic field direction is more often parallel to the shock normal at the dawn bow shock surface than at the dusk, the 'runaway' condition would be met more often there, a possible explanation for the stronger high-energy tail in the dawn magnetosheath.

Fourth, the energy densities of the low-energy and high-energy portions of the magnetosheath electron population are not independent; rather they (weakly) anticorrelate. This suggests a given amount of energy distributed between two populations rather than two independent populations superposed on one another.

*Acknowledgments.* The authors would like to thank William J. Burke and Thomas W. Hill for their helpful comments. The Imp 6 solar wind data were provided by W. C. Feldman, Los Alamos Scientific Laboratory. D. S. Colburn, NASA Ames Research Center, provided Explorer 35 magnetic field data. One of the authors (D. L. Reasoner) is currently a senior postdoctoral fellow at Marshall Space Flight Center, Huntsville, Alabama 35812. This work was supported by NASA contract NAS 9-5884 and NASA grant NSG-07025.

The Editor thanks S. J. Bame and J. D. Winningham for their assistance in evaluating this paper.

## REFERENCES

Akasofu, S. I., F. W. Hones, Jr., S. J. Bame, J. R. Asbridge, and A. J. Lin, Magnetotail and boundary layer plasmas at a geocentric distance of 18 $R_E$: Vela 5 and 6 observations, *J. Geophys. Res.*, *78*, 7257, 1973.

Bowling, S. B., and R. A. Wolf, The motion and magnetic structure of the plasma sheet near 30 $R_E$, *Planet. Space Sci.*, *22*, 673, 1974.

Burke, W. J., and D. L. Reasoner, Absence of the plasma sheet at lunar distance during geomagnetically quiet times, *Planet. Space Sci.*, *20*, 429, 1972.

Burke, W. J., J. J. Rich, D. L. Reasoner, D. S. Colburn, and B. J. Goldstein, Effects on the geomagnetic tail at 60 $R_E$ of the geomagnetic storm of April 9, 1971, *J. Geophys. Res.*, *78*, 8477, 1973.

Fenner, M. A., Magnetosheath plasma at 60 $R_E$, M.S. thesis, Rice Univ., Houston, Texas, 1971.

Fenner, M. A., Observations of magnetosheath plasma at the lunar orbit, Ph.D. thesis, Rice Univ., Houston, Texas, 1974.

Formisano, V., G. Moreno, F. Palmiotto, and P. C. Hedgecock, Solar wind interaction with the earth's magnetic field, 1, Magnetosheath, *J. Geophys. Res.*, *78*, 3714, 1973.

Goldstein, B. E., Observations of electrons at the lunar distance, *J. Geophys. Res.*, *79*, 23, 1974.

Hardy, D. A., H. K. Hills, and J. W. Freeman, Low-energy protons in the geomagnetic tail (abstract), *Eos Trans. AGU*, *56*, 390, 1974.

Howe, H. C., Jr., Explorer 33 and Explorer 35 plasma observations of the interaction region between the solar wind and the magnetic field of the earth, Ph.D. thesis, Mass. Inst. of Technol., Cambridge, Mass., 1971.

Howe, H. C., Jr., and J. H. Binsack, Explorer 33 and 35 plasma observations of magnetosheath flow, *J. Geophys. Res.*, *77*, 3334, 1972.

Montgomery, D., and G. Joyce, Shock-like solutions of the electrostatic Vlasov equation, *J. Plasma Phys.*, *3*, 1, 1969.

Moore, P. R., D. A. Hardy, and W. J. Burke, Low-energy plasma in the geomagnetic tail at lunar distance, 2, Joint observations (abstract), *Eos Trans. AGU*, *56*, 1168, 1974.

Reasoner, D. L., and W. J. Burke, Characteristics of the lunar photoelectron layer, *J. Geophys. Res.*, *77*, 6671, 1972.

Reasoner, D. L., and B. J. O'Brien, Measurement on the lunar surface of impact-produced plasma clouds, *J. Geophys. Res.*, *77*, 1292, 1972.

Rich, J. J., D. L. Reasoner, and W. J. Burke, Plasma sheet at lunar distance: Characteristics and interactions with the lunar surface, *J. Geophys. Res.*, *78*, 8097, 1973.

Scudder, J. D., D. L. Lind, and K. W. Ogilvie, Electron observations in the solar wind and magnetosheath, *J. Geophys. Res.*, *78*, 6595, 1973.

Spreiter, J. R., and A. Y. Alksne, Plasma flow around the magnetosphere, *Rev. Geophys. Space Phys.*, *7*, 11, 1969.

Vasyliunas, V. M., A survey of low-energy electrons in the evening sector of the magnetosphere with OGO 1 and OGO 3, *J. Geophys. Res.*, *73*, 2839, 1968.

Winningham, J. D., Characteristics of magnetosheath plasma observed at low altitudes in the dayside magnetospheric cusps, in *Earth's Magnetospheric Processes*, edited by B. M. McCormac, p. 68, D. Reidel, Dordrecht, Netherlands, 1972.

(Received September 24, 1974;
accepted December 2, 1974.)

*Proc. Lunar Sci. Conf. 6th* (1975), p. 2985–2993
Printed in the United States of America

# The effect of local magnetic fields on the lunar photoelectron layer while the moon is in the plasma sheet

WILLIAM J. BURKE,[1,2] PATRICIA H. REIFF,[1] and DAVID L. REASONER[1]

[1]Department of Space Physics and Astronomy, Rice University, Houston, Texas 77001

[2]Earth Observations Division, NASA Johnson Space Center, Houston, Texas 77058

Abstract—Data from the Charged Particle Lunar Environment Experiment, at the Apollo 14 site, are used to investigate the interactive properties of the plasma sheet and the lunar photoelectron layer. It is shown that the predictions of the Guernsey Fe model are compatible with SIDE but not CPLEE observations. The apparent contradiction is resolved by fitting the remanent magnetic field to that of a dipole buried ~ 1.1 km beneath the surface. In this case a charge separation layer must form above the instrument due to the different rigidities of plasma sheet electrons and protons. The qualitative properties of the charge separation layer needed to reconcile CPLEE and SIDE observations are presented.

## INTRODUCTION

FOR THE PAST FOUR YEARS charged particle fluxes in the immediate vicinity of the moon have been monitored by the lunar based Superthermal Ion Detector Experiment (SIDE), the Solar Wind Spectrometer (SWS), and the Charged Particle Lunar Environment Experiment (CPLEE). Each instrument has unique detection capabilities. It is only by comparing information slowly gained from the various instruments that a coherent picture of particle interactions with the moon can be constructed. In the quest for synthesis, we undertake an examination of the interactions of the plasma sheet and the lunar photoelectron layer. The Apollo 14 based CPLEE is our principal source of data. Yet, as it emerges from our analysis, without information gained by SIDE and the SWS the whole story cannot be told. In fact, CPLEE data alone leads us into an unresolvable paradox.

Reasoner and Burke (1972) have reported on lunar photoelectrons observed by CPLEE in the high latitude lobes of the geomagnetic tail. The photoelectron spectrum was shown to be isotropic and has a power law distribution in the energy range 40–200 eV. The power law distribution was found by Goldstein (1974), using SWS data, to continue down to 5 eV. Laboratory studies of photoelectrons emitted from lunar fines suggest that the spectrum has a maximum between 1 and 2 eV (Feuerbacher *et al.*, 1972). With this base information we should be able to calculate the potential distribution under a wide variety of external plasma conditions.

Local magnetic fields, observed by the Lunar Portable Magnetometer (LPM) and Lunar Surface Magnetometer (LSM) at the Apollo 12, 14, and 15 sites, have been reported by Dyal *et al.* (1970, 1971, 1972). LSM measurements at the Apollo 12 site show a local field of 38 γ directed toward the surface and the southeast. In



PRECEDING PAGE BLANK NOT FILMED

ORIGINAL PAGE IS
OF POOR QUALITY

the plane tangent to the surface the field gradient is $\sim 0.4$ gamma/m. Two measurements separated by 1.1 km at the Apollo 14 site show local remnant fields of 103 $\gamma$ directed toward the surface and the southeast, and 43 $\gamma$ directed toward the surface and the southwest. A very weak field of 6 $\gamma$, directed toward the vertical and south southeast, was observed at the Apollo 15 site.

In the following section we consider CPLEE plasma sheet data in comparison with the potential minimum model proposed by Guernsey and Fu (1970). Although the predictions of this model are in accord with recently reported SIDE plasma sheet observations (Freeman and Ibrahim, 1974) made at the Apollo 14 and 15 sites they cannot explain CPLEE observations. An appeal to currents generated by secondary electrons is then shown incapable of resolving the paradox. The effects of local magnetic fields on particle trajectories are then investigated. It is found that due to the differential stopping power of the magnetic field with respect to incident protons and electrons a charge separation layer must exist above the Apollo 14 site similar to that deduced from comparisons of Apollo 12 SWS data with satellite (Neugebauer *et al.*, 1972) and Apollo 15 SWS observations (Goldstein, 1974). The properties of the charge separation layer are investigated and are shown to be capable of resolving the SIDE–CPLEE paradox.

## A Lunar Surface Potential Calculation

A complete description of the CPLEE instrument has been given by Burke and Reasoner (1972). Briefly, CPLEE contains two identical sets of electrostatic analyzers, *A* and *B*, capable of measuring a 15 point spectrum of electron and proton fluxes with energies between 40 eV and 20 keV every 19.2 sec. Analyzer *A* looks toward local vertical and analyzer *B* looks in a direction 60° from vertical toward lunar west. The instrument was deployed on February 5, 1971. Analyzer *B* failed on April 8, 1971, while analyzer *A* collected data until the central station failure in March, 1975.

A quiet time plasma sheet spectrum, observed by CPLEE's analyzer *A*, has been reported by Rich *et al.* (1973), and is reproduced as Fig. 1. During magnetically quiet times particle densities are observed to be approximately 0.1 $cm^{-3}$. The electron and proton temperatures are $\sim 200$ eV and 2.5 keV, respectively. Proton fluxes are found to be the same in analyzers *A* and *B*. With notable exceptions the plasma sheet electron fluxes are greater in analyzer *A* and *B*. Because strong electron anisotropies are unstable, Rich *et al.* (1973) maintained that at lunar distance plasma sheet fluxes are isotropic.

The fluxes of electrons with energies $\gtrsim 80$ eV, in Fig. 1, are of plasma sheet origin while those with energies less than $\sim 80$ eV are photoelectrons generated at the lunar surface. Generally while in the plasma sheet, the photoelectron counting rates are elevated by $\lesssim 50\%$ relative to their high-latitude tail values. The disappearance of photoelectrons has been observed in the presence of intense plasma sheet fluxes accompanying the magnetic storms of April 9, 1971 (Reasoner and Burke, 1972) and January 19, 1973 (Moore *et al.*, 1974). The simplest interpretation of the quiet and magnetically disturbed observations is: Analyzer *A*

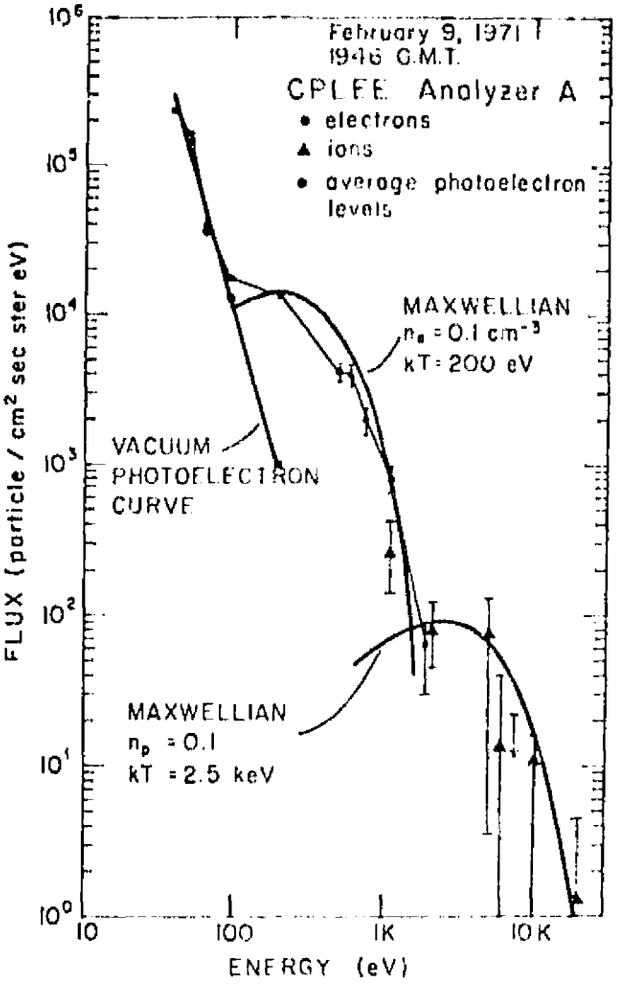


Fig. 1. Spectrum observed by CPLEE's analyzer *A* while in the plasma sheet. Fluxes of electrons with energies $\leq 80$ eV are from photoelectrons while those with energies $\geq 80$ eV are of plasma sheet origin.

is looking at downwelling fluxes of photoelectrons which must be trapped during quiet times by a surface potential of $-80$ volts. During disturbed times the intense fluxes of plasma sheet electrons drives the surface potential below 40 volts allowing photoelectrons with energies observable by CPLEE to escape. In order to test this interpretation we have calculated the electrostatic potential distribution near the surface of the moon using the Guernsey and Fu (1970) potential minimum model. The plasma sheet and photoelectron distributions are taken from CPLEE and SWS observations.

For the sake of simplicity in our calculations of the near lunar surface potential

distribution, we assume that:

(1) The sunlit hemisphere may be approximated by a flat photoemitting plate. Thus, the potential is only a function of height above the surface.
(2) In the plasma sheet the moon is embedded in a magnetic field with straight line geometry, aligned perpendicular to the surface.
(3) All plasma sheet particles striking the lunar surface are absorbed.
(4) There is a continuous supply of plasma sheet electrons and protons.

The fourth assumption conforms to CPLEE's observation of plasma sheet particles for periods in excess of an hour.

The Guernsey–Fu model assumes that the surface potential of the sunlit hemisphere $\phi_0 > 0$. Above the surface the potential falls to a minimum value $\phi_m \leq 0$. If $\phi_m = 0$, the potential remains zero as $x \to \infty$. If $\phi_m < 0$ the potential returns to zero as $x$ approaches $\infty$. (Here $x$ represents height above the surface.) The boundary conditions which the calculation must satisfy are

(1) Equal densities of electrons and protons at $x = \infty$.
(2) The current density is zero throughout the entire system.
(3) The electric field vanishes at $x = -\infty$.

At $x = +\infty$, the electron population consists of plasma sheet electrons injected into the tube of flux and those reflected by the potential minimum barrier, plus photoelectrons that have escaped the moon. The proton population consists of injected and reflected plasma sheet particles. Poisson's equation and the flux balance equation are needed to calculate the potential distribution. The solutions depend only on the distributions of the plasma sheet particles injected at $x = \infty$ and of the photoelectrons emitted at $x = 0$. In conformity with CPLEE observations we represent the injected electrons and protons with Maxwellian distributions that are isotropic over the down moving hemisphere

$$f_e(v, x) = \begin{cases} 0 & 0 \leq \theta \leq \dfrac{\pi}{2} \\ \dfrac{2n_e(\infty)}{\pi^{3/2}\omega_e^3}\, e^{-v^2/\omega_e^2} & \dfrac{\pi}{2} < \theta \leq \pi \end{cases} \tag{1}$$

and

$$f_i(v, x) = \begin{cases} 0 & 0 \leq \theta \leq \dfrac{\pi}{2} \\ \dfrac{2n_i(\infty)}{\pi^{3/2}\omega_i^3}\, e^{-v^2/\omega_i^2} & \dfrac{\pi}{2} < \theta \leq \pi \end{cases} \tag{2}$$

where $n_e(\infty) = n_i(\infty) = 0.1\ \text{cm}^{-3}$; $\omega_e$ and $\omega_i$ are the thermal velocities associated with electron and proton temperatures of 200 eV and 2.5 keV, respectively. $\theta$ is the angle between the particle's velocity and the positive $x$ axis. The power law

spectrum observed in the SWS and CPLEE photoelectron data suggests that the distribution of upwelling photoelectrons at the surface can be represented by a kappa function (Vasyliunas, 1968)

$$f_e(v,0) \quad \frac{n_e(0)\Gamma(\kappa+1)}{(\pi\kappa)^{3/2}\Gamma\left(\kappa-\frac{1}{2}\right)\omega_e^3}\left[1+\frac{v^2}{\kappa\omega_e^2}\right]^{\kappa+1} \tag{3}$$

where $\omega_e$ is the most probable thermal velocity and $\kappa$ is the spectral slope at high energies. The energy spectrum derived from this distribution with $n_e(0) = 239$, $\frac{1}{2}m\omega_e^2 = 0.8$ eV and $\kappa = 3$ is shown in Fig. 2. A comparison with laboratory and *in*

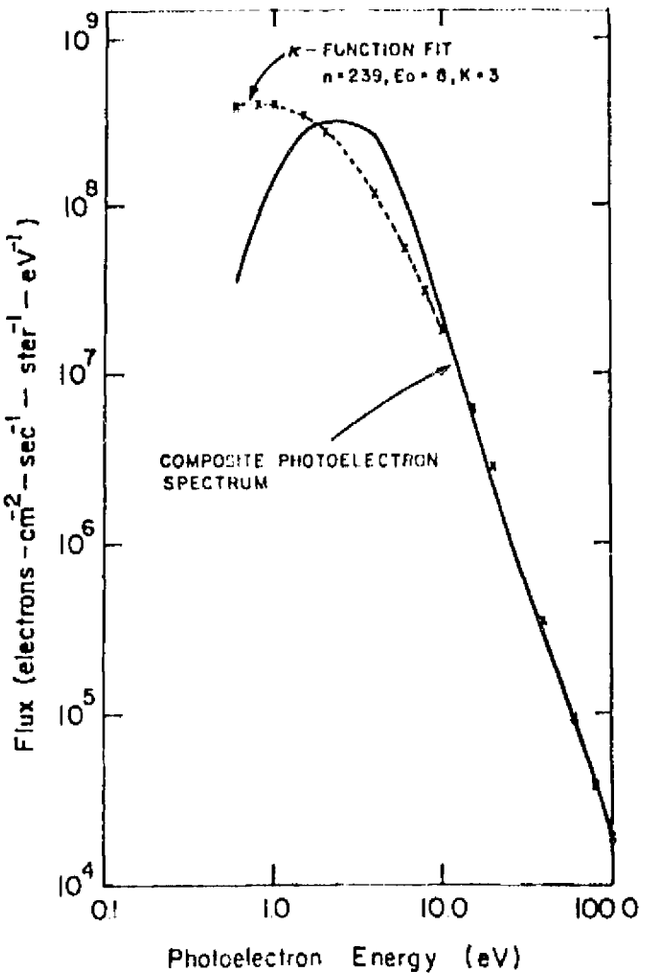


Fig. 2. Composite photoelectron spectrum using kappa function fit

*situ* observations shows that for particles with energies greater than 10 eV the fit is excellent. Although the fit below 10 eV is rather poor, for surface potentials greater than 10 volts, the lower energy particles do not contribute to the current balance calculations. In this case the distribution in Eq. (3) can be used with only a small error.

These distributions have been used to solve the flux balance and Poisson equations by numerical analysis. The results shown in Fig. 3 plot the potential minimum as a function of the surface potential. The simultaneous solution of the two equations occurs at $\phi_0 = 7.9$ volts and $\phi_m = -3.6$ volts. Thus photoelectrons with $\frac{1}{2}MV_x^2 > 11.5$ volts escape the moon. On the basis of this calculation, we argue that the spectrum of downwelling electrons should be similar to that sketched in Fig. 4 rather than that observed in Fig. 1.

The most obvious escape from this dilemma is to argue that we have ignored the effects of secondary electrons produced by plasma sheet particles striking the lunar surface. CPLEE data show that photoelectrons must overcome a barrier of ~80 volts in order to escape the lunar surface. Thus only secondary electrons with energies in excess of 80 eV may contribute to the return current. Laboratory studies of secondary electrons from lunar fines generated by primary electrons with plasma sheet energies have maximum energies < 50 eV (Anderegg *et al.*, 1972). Protons with energies of a few kilo electron volts, when bombarding certain

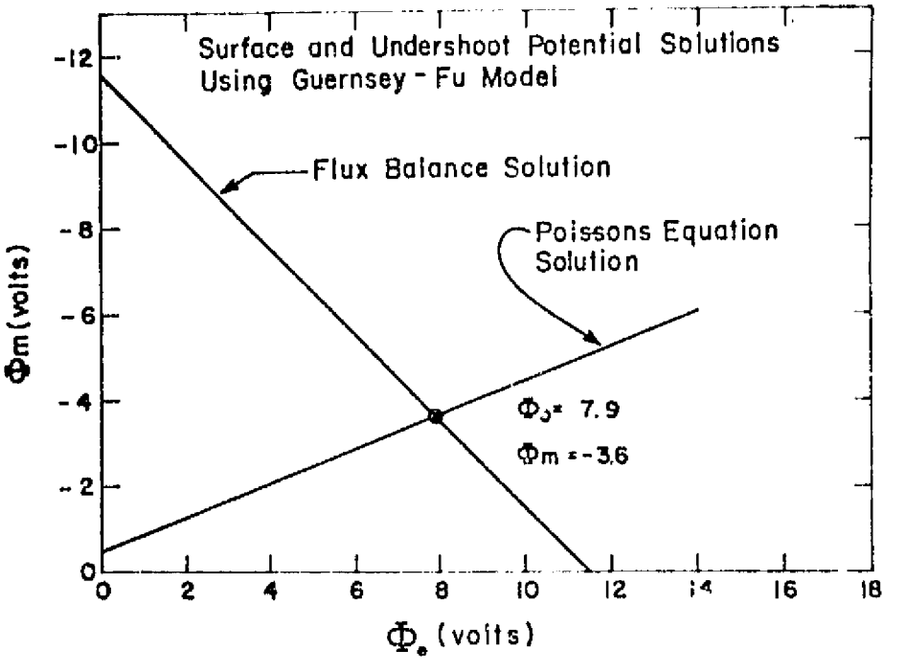


Fig. 3. Solutions of the flux balance and Poisson equations for the Guernsey–Fu model. Plasma and photoelectron parameters were taken from CPLEE and SWS observations.

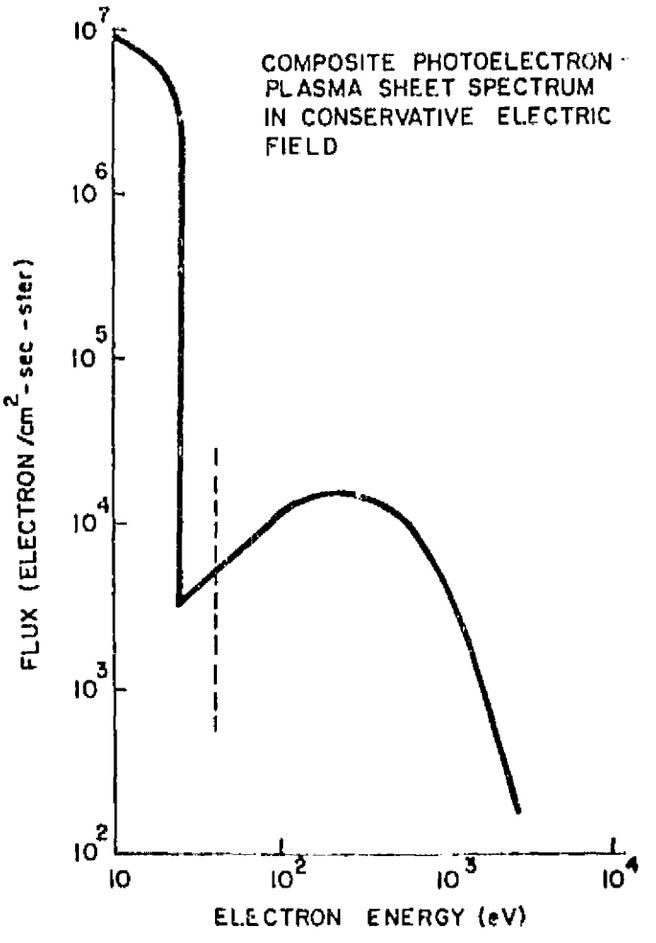


Fig. 4. Sketch of electron spectrum predicted by Guernsey-Fu model for the moon in the plasma sheet

dielectric and conducting surfaces, are efficient producers of secondary electrons with energies in excess of 100 eV (Carter and Colligon, 1968). Unfortunately, the spectrum of secondary electrons from lunar fines due to ion bombardment has never been investigated. Our calculations show that plasma sheet protons would have to produce 0.78 secondary electrons with energies greater than 80 eV per incident proton in order to bring CPLEE observations in line with the predictions of the potential minimum model. Such an efficiency is deemed unlikely.

Recently Freeman and Ibrahim (1974) have reported observing surface potentials near 10 volts with SIDE detectors at the Apollo 14 and 15 sites while the moon was in the plasma sheet. The SIDE method of measuring surface potentials is described by Freeman *et al.* (1973). In summary form: Ions are created by the

photoionization of thermal neutrals in the lunar atmosphere. When the SIDE stepping plate is set at negative voltages relative to ground, these ions are accelerated into the detector where they are observed as a resonance if there is an energy channel near $-q(\phi_{sp}+\phi_0)$. $\phi_{sp}$ is the stepping plate potential and $\phi_0$ the surface potential. While it was gratifying to see that the potential minimum model calculations were compatible with SIDE data, these observations tended to underscore the mysterious nature of the CPLEE observations.

## Effects of the Local Magnetic Field

To this point in our calculation, the effects of local magnetic fields have been ignored. This approximation is valid if the gyroradii of the electrons in question are large in comparison with the local magnetic field scale size. The average value of the magnetic field measured at two Apollo 14 sites was $\sim 75\,\gamma$ with a scale length of $\sim 0.8$ km (Dyal *et al.*, 1972). Thus electrons with $E \simeq 320$ eV are sufficiently perturbed by this field to make its neglect unwarranted in the analysis of CPLEE data.

In order to approximate the magnetic field in the vicinity of the ALSEP site we assume that the two vector magnetic field measurements resulted from a dipole beneath the lunar surface. The dipole needed to fit the measured fields must be of strength $8.0\times10^5$ gauss-m$^3$, oriented vertically down at a depth of $\sim 1.1$ km beneath the intersection of the horizontal field components measured at Sites A and C. The geometry of the situation is sketched in Fig. 5. Under the dipole assumption the field strength of CPLEE is $\sim 75\,\gamma$ with an orientation shown in Fig. 5.

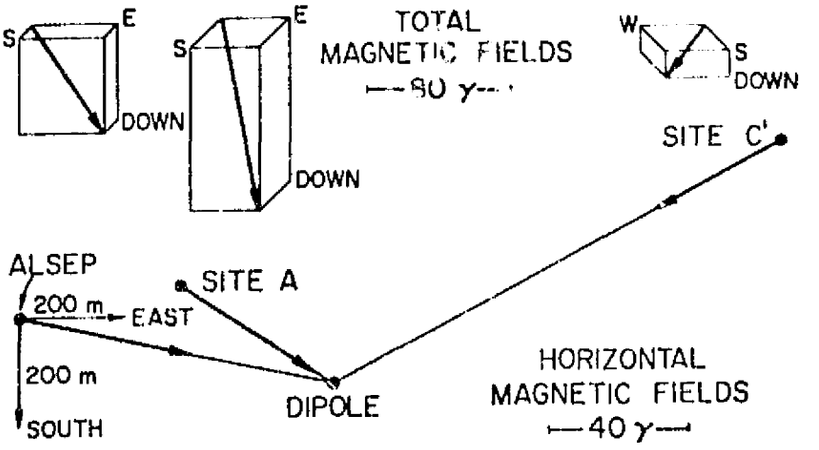


Fig. 5. Remnant magnetic fields in the vicinity of the Apollo 14 site. The horizontal components of the fields measured at sites A and C' are used to locate the dipole. Under the dipole assumption a field of 75 γ was calculated near CPLEE.

The meridianal plane trajectories (Störmer, 1955) of electrons reaching CPLEE's analyzer *A* were computed (Reiff, 1975). These calculations show that: (1) all electrons reaching the detector approached it from weaker regions of dipole field; (2) with some external field orientations and a surface potential of 10 volts, the flux of photoelectrons with energies near 40 eV could be explained in terms of magnetic mirroring. This mechanism cannot explain observed fluxes of downwelling photoelectrons in the 50- and 70-eV channels.

The effects of the local magnetic field at the Apollo 12 site on solar-wind and magnetosheath particles reaching the lunar surface have been investigated by Neugebauer *et al.* (1972) and Goldstein (1974). Neugebauer *et al.* (1972) have shown that differences between OGO3 and the Apollo 12 SWS solar-wind proton observations can be explained only if the existence of a charge separation layer above the surface is postulated. Further evidence for the existence of such a layer was found in SWS magnetosheath electron fluxes. Comparing Apollo 12 with Apollo 15 SWS data Goldstein found that Apollo 12 electrons had been accelerated by as much as 170 volts. A somewhat qualitative description of the formation of the charge separation layer, due to the different penetration distances of protons and electrons, has been put forth by Siscoe and Goldstein (1973).

By postulating the existence of a charge separation layer in the magnetic field above the Apollo 14 site, the mysterious qualities of CPLEE become intelligible. The geometric features of the layer are similar to Siscoe and Goldstein's mode 1 with particles hitting the surface. A major difference is that the external plasma is isotropic rather than highly directed.

The scale length of the Apollo 14 field is small. In the dipole approximation, local magnetic field above CPLEE falls to 10 $\gamma$, about twice the ambient plasma sheet magnetic field, at a height of ~ 1 km. From this height down the guiding center approximation is no longer valid for all protons and most electrons. Essentially all protons reach the surface, whereas low-energy electrons are reflected by the magnetic field. An estimate of the charge separation potential can be gained by making the assumption that a certain fraction of the incident electrons are turned around at a height $h$ above CPLEE. In the zero-order approximation (Reiff, 1975) we assume a surplus positive charge density $\rho$ that is constant from $x = 0$ to $x = h$. The solution to Poisson's equation

$$\phi(x) = a_0 + a_1 x - \frac{\rho}{\epsilon_0} x^2 \qquad (0 \le x \le h)$$

is subject to the boundary condition of no external electric fields (i.e. $x_1 = 0$) and $\phi(h) = 0$. Thus

$$\phi(x) = \phi_{cs}\left(1 - \frac{x^2}{h^2}\right)$$

where $\phi_{cs} = \rho h^2/\epsilon_0$ is the total potential difference due to the charge separation. For a charge separation potential $\phi_{cs} = 50$ volts beginning at a height of 1 km the proton charge density must exceed that of the electrons by 2.8%. This is approximately the density difference one would expect from flux balance at $h$.

ORIGINAL PAGE IS
OF POOR QUALITY

With an ambient plasma sheet density of $\sim .1$ cm$^{-3}$, however, such a perturbation could not be detected by CPLEE. A sketch of the potential distribution as a function of height with $h = 1$ km is shown in Fig. 6a. Because the photoelectron potential extends for only a few meters above the surface it appears as a spike on top of the charge separation potential.

We now turn our attention to the SIDE resonance phenomena. Based on shielding lengths calculated for the high-latitude tail photoelectron layer, we estimate the SIDE shielding distance to be of the order several meters to several tens of meters. The potential distribution above SIDE at the Apollo 14 site is sketched in Fig. 6b, for a zero ground step (dashed) and negative step (solid). The effects of the photoelectric surface potential are felt out to a height of $\sim 10$ m. Above this height the potential is approximately constant out to a height of $\sim 20\%$ of the height of the charge separation layer. Ions created in the plateau region of the potential can be detected by SIDE. Photoelectrons with surface energies less than the total potential, $\phi_{ps} + \phi_{cs}$ are reflected to the surface; those with greater energies escape.

The actual strength of the potential difference across the separation layer can be estimated from CPLEE observations. For favorable external magnetic field conditions the potential barrier is observed to be about 50–70 volts. A potential barrier in excess of 100 volts was observed during a substorm. These potential differences are smaller than those observed by Goldstein at the Apollo 12 site. We attribute the difference to the smaller magnetic field scale length near Apollo 14.

One final consequence of this model is an explanation of the observed elevation of photoelectron potential observed by CPLEE in the plasma sheet. The Störmer trajectory analysis revealed that all photoelectrons reaching our analyzers came from weaker regions of the magnetic field. In weaker regions of the magnetic field the flux of plasma sheet electrons reaching the surface should be greater than near CPLEE. Thus, the surface potential in the regions where the photoelectrons originate should be lower. A comparison of the distribution functions observed in the high-latitude tail and the plasma sheet, in conjunction with the Liouville theorem, can be used to calculate the potential difference between CPLEE and the point of origin. The potential difference is $\sim 4$ volts. Unfortunately it is not until after we have calculated the self-consistent charge separation layer that we can know the photoelectron's point of origin. Based on field scale length considerations we would expect it to be of the order of a few hundred meters from CPLEE.

## Summary and Conclusions

In this paper we have tried to bring some degree of unity to reported observations of SIDE, SWS, and CPLEE. Data from SWS have been used, in conjunction with laboratory observations, to estimate the distribution function of the photoelectrons emitted by the lunar surface. The potential distribution near the surface of the moon was calculated with the help of this distribution function. This calculation is found to be in substantial agreement with plasma sheet

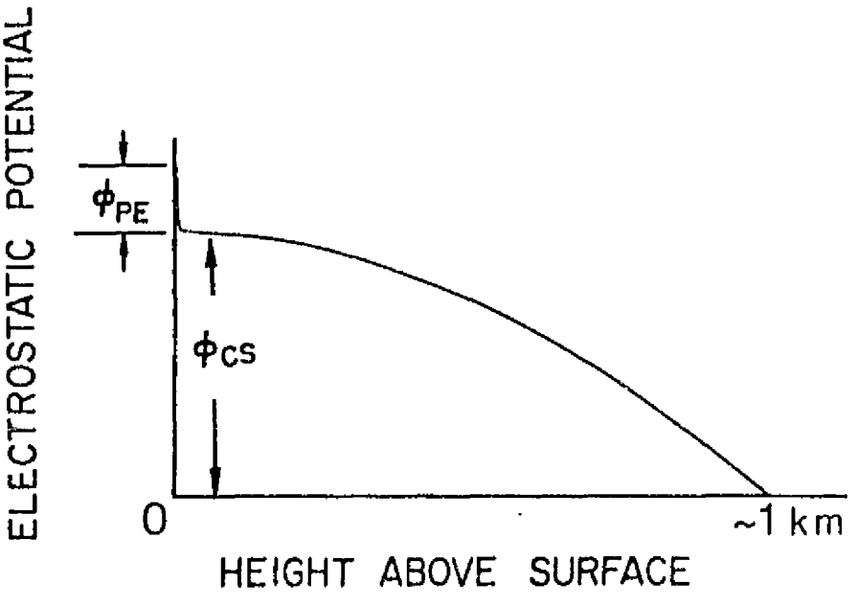


Fig. 6a. Potential distribution near the lunar surface. The potential drop near the surface is that necessary to satisfy zero net current into the surface. The drop at the higher altitude is due to the charge separation layer.

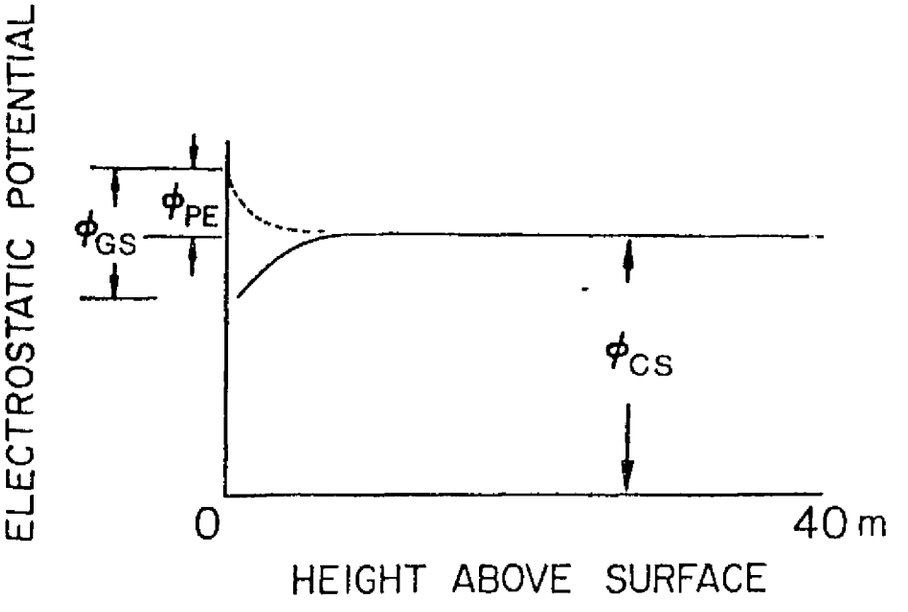


Fig. 6b. Expansion of Fig. 6a to low altitudes (dashed). The solid curve is the expected potential distribution above SIDE with a negative ground stepper voltage ($\Phi_{gs}$).

observations made by SIDE at the Apollo 14 and 15 sites. It is however at variance with CPLEE observations of downwelling fluxes of ~80-eV photoelectrons under similar conditions.

The two vector magnetic field measurements at the Apollo 14 site have been fit to the field of a dipole buried beneath the surface. When combined with the external magnetic field we find agreement between CPLEE's predicted and observed shadow zones. A consequence of the interaction of plasma sheet particles with the field is the formation of a charge separation region above the Apollo 14 site similar to that observed by SWS at Apollo 12. The concept of a charge separation region is found capable of resolving the apparently divergent observations of CPLEE and SIDE. Near the lunar surface the potential distribution would be similar to that predicted by the Guernsey–Fu model. Thus SIDE observes a surface potential ~10 volts at Apollo 14 and 15 sites. The charge separation region above the Apollo 12 and 14 sites reflects photoelectrons with energies less than the total potential barrier to the surface. It must be part of our ongoing research to develop a mathematically self-consistent potential distribution out of the qualitative model that we have here presented.

## REFERENCES


Anderegg M., Feuerbacher B., Fitton B., Laude L. D., and Willis R. F. (1972) Secondary electron emission characteristics of lunar fines. *Proc. Lunar Sci. Conf. 3rd*, p. 2655–2664.

Burke W. J. and Reasoner D. L. (1972) Absence of the plasma sheet at geomagnetically quiet times. *Planet. Space Sci.* 20, 429–436.

Carter G. and Colligon J. S. (1968) *Ion Bombardment of Solids*, p. 38–74. American Elsevier, New York.

Dyal P., Parkin, C. W., and Sonett C. P. (1970) Lunar surface magnetometer experiment. In *Apollo 12 Preliminary Sci. Report*, NASA publication SP-235, p. 55–73.

Dyal P., Parkin C. W., Sonett C. P., DuBois R. L., and Simmons G. (1971) Lunar portable magnetometer experiment. In *Apollo 14 Preliminary Sci. Report*, NASA publication SP-272, p. 2-27 to 2-37.

Dyal P., Parkin C. W., and Sonett C. P. (1972) Lunar-surface magnetometer experiment. In *Apollo 15 Preliminary Sci. Report*, NASA publication SP-289, p. 9-1 to 9-16.

Feuerbacher B., Anderegg M., Fitton B., Laude L. D., and Willis R. F. (1972) Photoemission from lunar fines. *Proc. Lunar Sci. Conf. 3rd*, p. 2655–2664.

Freeman J. W. and Ibrahim M. E. (1974) The lunar electric potential and its plasma sheath effects (1). In *Interactions of the Interplanetary Plasma with the Ancient and Modern Moon*, p. 87–88. The Lunar Science Institute, Houston.

Freeman J. W., Fenner M. A., and Hills H. K., (1973) Electric potential of the moon in the solar wind. *J. Geophys. Res.* 78, 4560–4567.

Goldstein B. E. (1974) Observations of electrons at the lunar distance. *J. Geophys. Res.* 79, 23–35.

Guernsey R. L. and Fu J. H. M., (1970) Potential distribution surrounding a photoemitting plate in a dilute plasma. *J. Geophys. Res.* 75, 3193–3199.

Moore P. R., Hardy D. A., and Burke W. J. (1974) Low-energy plasma in the geomagnetic tail at lunar distance: II, joint observations (abstract). *EOS (Trans. Amer. Geophys. Union)* 56, 1168.

Neugebauer M., Snyder C. W., Clay D. R., and Goldstein B. E. (1972) Solar wind observations on the lunar surface with the Apollo 12 ALSEP. *Planet. Space Sci.* 20, 1577–1591.

Reasoner D. L. and Burke W. J. (1972) Characteristics of the lunar photoelectron layer. *J. Geophys. Res.* 77, 6671–6687.

Reiff P. H. (1975) Modification of particle fluxes at the lunar surface by electric and magnetic fields. Ph.D. thesis, Rice University, Houston, Texas.

Rich F. J., Reasoner D. L., and Burke W. J. (1973) Plasma sheet at lunar distance: Characteristics and interaction with the lunar surface. *J. Geophys. Res.* 78, 8097–8112.

Siscoe G. L. and Goldstein B. E. (1973) Solar wind interaction with lunar magnetic fields. *J. Geophys. Res.* 78, 6741–6748.

Störmer C. (1955) *The Polar Aurora*. Oxford University Press, Fair Lawn, N.J.

Vasyliunas V. M. (1968) A survey of low-energy electrons in the evening sector of the magnetosphere with OGO-1 and OGO-3. *J. Geophys. Res.* 73, 2839–2884.

*Proc. Lunar Sci. Conf. 6th* (1975), p. 3023–3032
Printed in the United States of America

# Lunar nightside electron fluxes

DAVID L. REASONER

NAS/NRC Senior Postdoctoral Fellow,* NASA/Marshall Space Flight Center, Huntsville, Alabama 35812

**Abstract**- Studies of particle fluxes at the lunar surface with the Apollo 14 ALSEP/C PLEE particle spectrometer during lunar night periods have shown three distinct types of electron flux events. One of these is shown to originate at the earth's bow shock, but the remaining two are shown to arise most likely as a result of local solar wind–lunar interactions. The flux events had mean electron energies of a few hundred electron volts and total fluxes of $10^6$–$10^7$ electrons/cm$^2$ sec. These fluxes are a possible source of the large negative lunar surface potentials observed by other ALSEP instruments.

## I. INTRODUCTION

OBSERVATIONS OF CHARGED PARTICLE FLUXES at and near the lunar night surface when the moon was in the solar wind have shown that the so-called "downstream plasma void cavity" is a misnomer and that indeed significant charged particle fluxes are present in this region. For example, Anderson *et al.* (1972) have detected electrons with $E > 500$ eV in the cavity with the lunar-orbiting Particles and Fields Subsatellite, while energetic ion bursts at the lunar night surface have been detected with the ALSEP/SIDE instruments (Freeman, 1972).

In a recent paper (Reasoner, 1975) we reported on observations by the CPLEE lunar surface ion–electron spectrometer of electron fluxes at the nightside lunar surface while the moon was upstream of the earth in the solar wind. In that paper we showed that a subset of observed electron fluxes were strongly controlled by the direction of the interplanetary magnetic field (IMF), appearing at the moon only when the moon was connected to the earth's bow shock along magnetic field lines. We therefore proposed that these electrons were generated at the bow shock and subsequently propagated back upstream to the lunar surface. The densities and temperatures of these electron fluxes were in the ranges $2–4 \times 10^{-1}$ cm$^{-3}$ and $1.7–2.8 \times 10^{5}$°K. The fluxes were then in the range $0.4–1.0 \times 10^6$ electrons/cm$^2$-sec.

The implications of these observations are discussed by Reasoner (1975). To summarize briefly, Scudder *et al.* (1973) observed small enhancements in the measured solar-wind electron temperature when the OGO-5 satellite was upstream of the earth and connected to the bow shock along magnetic field lines. We asserted that these bow shock electrons observed at the lunar surface were responsible for the solar-wind electron temperature increases. The moon acted to shield the instrument from the direct solar wind and allowed an uncontaminated

*On leave from Rice University, Houston, Texas.



PRECEDING PAGE BLANK NOT FILMED

measurement of these bow shock electrons. If it is assumed that the electrons are the high-energy tail of the magnetosheath electron distribution, then the total potential barrier through which the electrons had to travel from the downstream side of the shock to the lunar surface (bow shock potential plus lunar surface potential) is estimated to be 500 volts.

In this paper we extend the observations of lunar nightside electron flux events to include two other types, distinguished by their phenomenological characteristics, which also make significant contributions to the total charged particle flux to the nightside lunar surface. These other two types of flux events, in contrast to the Type I bow shock flux events reported earlier, are shown to arise most likely as a result of lunar-solar wind interactions. The implications of these flux events to the problem of the lunar nightside surface potential will also be discussed.

## II. Observations

The electron flux measurements were made with the Charged Particle Lunar Environment Experiment (CPLEE), a component of the Apollo 14 ALSEP system. A complete instrument description may be found in Burke and Reasoner (1972). The instrument was sensitive to electrons with energies ranging from 40 to 20 keV, and for this study the 8 lower energy channels ranging from 40 to 700 eV will be used. Magnetic field data from the Explorer 35/Ames Research Center magnetometer in lunar orbit provided magnetic field line geometry information.

Data from four contiguous lunar night periods from February to May 1971 were examined for the presence of electron fluxes. It was found that there were sporadic, though significant, fluxes of electrons impacting the lunar surface throughout the lunar night. Figure 1 shows an example of the lunar night flux events. These data were from May 25, 1971. On this day the solar ecliptic longitude of the moon ranged from 4° to 16°, i.e. the moon was almost directly upstream of the earth and the instrument was located 16° to 4° from the lunar midnight meridian toward the dusk terminator. In this figure the lower panel shows the counting rate from the 200-eV electron channel of the instrument. This channel was chosen because of its larger geometric factor and consequent higher counting rates. The upper two panels are the solar ecliptic latitude ($\theta$) and the solar ecliptic longitude ($\phi$) of the interplanetary magnetic field. The data gaps in the magnetometer record are due to the operational characteristics of the Explorer 35 satellite. Also shown on the figure (dotted lines) are the boundaries of the regions in $\phi$ where the IMF lines connect from the moon to the earth's bow shock. For values of $\phi$ between the boundaries (near $\phi$ 0°) the moon is connected to the bow shock.

The two large flux events centered at 0215 and 0330 are examples of Type I flux events as evidenced by the correlation between occurrences of the fluxes and the IMF direction. However, it is seen that at other times, for example around 1200, there are electron flux events which are present even when there is no IMF connection from the moon to the bow shock. Although the occurrence of these events is sporadic, the event-to-event intensity displays no systematic changes

ORIGINAL PAGE IS
OF POOR QUALITY

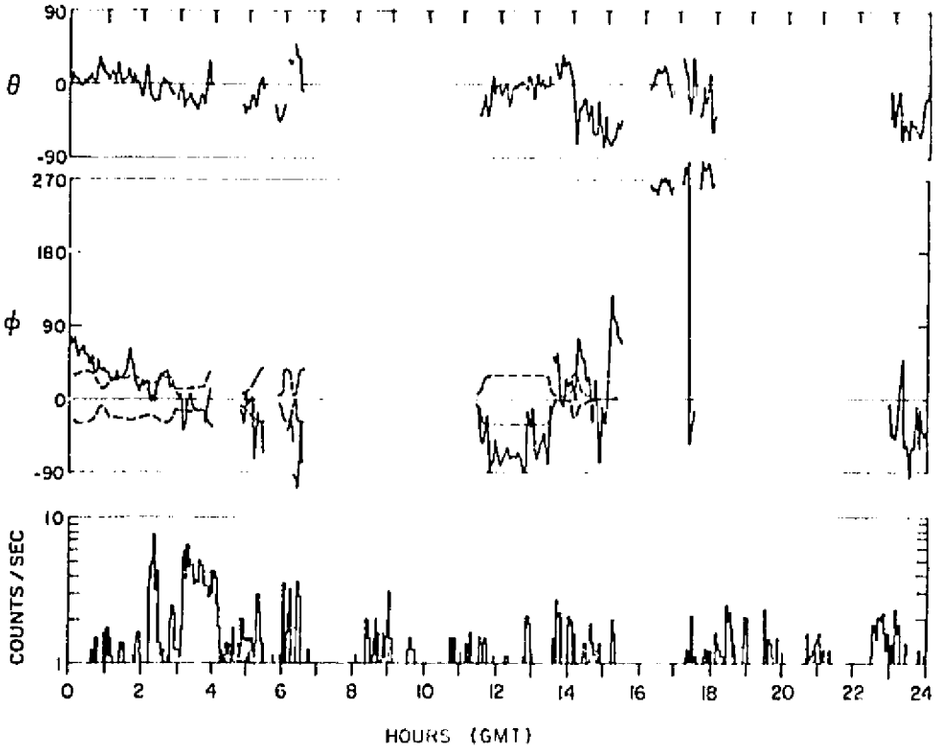


Fig. 1. Electron flux and magnetic field data for May 25, 1971 when the CPLEE instrument was on the nightside lunar surface near lunar midnight. The bottom panel shows the counting rate due to 200 eV electrons, and the top two panels show the solar ecliptic latitude ($\theta$) and longitude ($\phi$) of the interplanetary magnetic field. The dotted lines on the $\phi$ plot delineate the zones of IMF connection from the moon to the earth's bow shock. This figure illustrates Type I and Type II lunar nightside electron flux events.

with distance of the instrument from the lunar terminator. We refer to these events as Type II.

The distinction between Type I and Type II events is based both on the dependencies on IMF direction and on their relative intensities. In the data base analyzed, a total of 14 events were identified and classified as Type I based on their correlation with IMF direction. For each of the 14 events the data were searched for the nearest flux event which met the criterion that the IMF direction must have been such that the moon was not connected to the bow shock. The maximum 10-min average counting rates in the 200 eV channel were then tabulated for the two sets of events, and the averages ($\bar{C}R$) and standard deviations (S) were calculated. The mean and standard deviation for the bow shock-connected events were $\bar{C}R = 5.04$ and $S = 1.52$, and for the non bow shock-connected events the mean and standard deviation were $\bar{C}R = 2.25$ and $S = 0.27$.

The normalized difference of the means is 6.7, and hence we conclude that there is a statistically significant difference in the intensity of lunar night electron flux events depending on whether or not the moon is connected to the earth's bow shock along the IMF lines.

Figure 2 shows an example of a third type of lunar nightside electron flux event. Here, as in Fig. 1, the counting rate of the 200 eV electron channel is displayed. Also shown is the geomagnetic disturbance parameter *Kp*. The data displayed cover the period from 1200 U.T. on May 18, 1971 (Day 138) to 0000 U.T. on May 23 (Day 143). Lunar sunset, marked by an arrow and the corresponding disappearance of lunar photoelectron fluxes, occurred at 1930 U.T. on May 18 (Day 138). Electron fluxes are seen at the terminator and to persist into the lunar night period for approximately 4 days but with gradually decreasing intensity. The corresponding behavior is also seen prior to dawn terminator crossing, i.e. these fluxes first appear approximately 4 days prior to crossing. These fluxes are distinguished by their greater intensity than either the Type I or Type II events discussed earlier; and, unlike the other two types, they are strongly correlated with *Kp*. As can be seen from the figure, the fluxes are absent when *Kp* is below 1+. Although the connection between the geomagnetic activity index *Kp* and

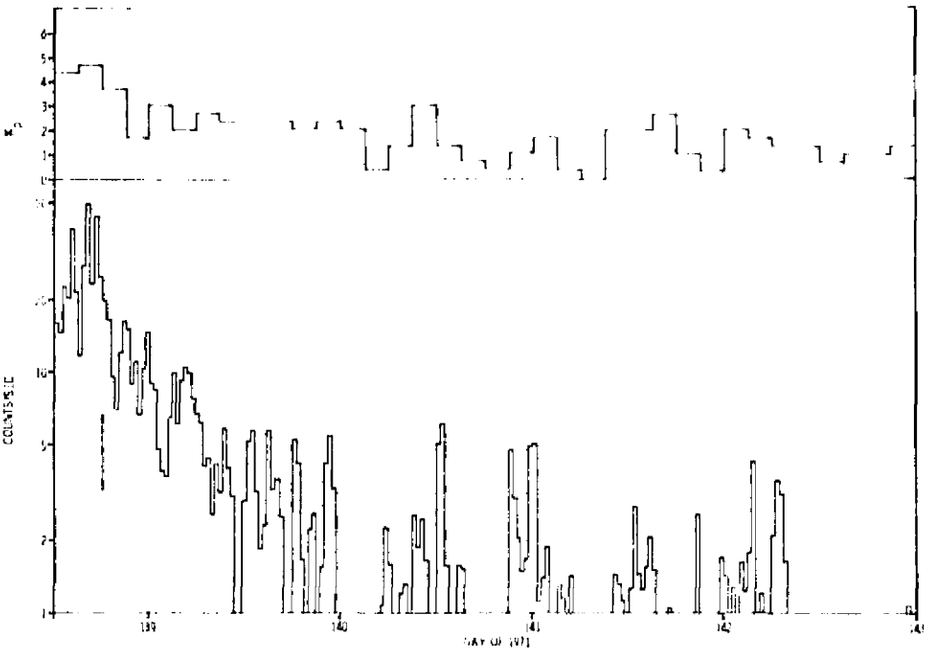


Fig. 2. Electron flux and *Kp* data for the period May 18–May 23, 1971 (Day 138–143) when the instrument was crossing the dusk terminator and proceeding into the lunar nightside. Sunset is marked by the vertical arrow on May 18 at 1930 hr. This figure illustrates Type III flux events and shows their correlation with *Kp*

events at the moon far upstream of the earth may not be obvious, $Kp$ has been shown to be an indirect indicator of the velocity of the solar wind (Snyder *et al.*, 1963). Thus these Type III fluxes appear to originate at or near the lunar terminators and are influenced by solar-wind conditions. The occurrence, if any, of these fluxes at the lunar dayside surface is impossible to determine since they are considerably weaker than the photoelectron fluxes observed at the surface on the sunlit hemisphere (Reasoner and Burke, 1972) and would be masked by the photoelectrons.

Electron spectra for the longer duration electron flux events were computed from 30-min averages. These long averages were necessary to gain statistical significant in view of the low counting rates of the electron flux events. Background subtraction corrections and standard deviations were computed by fitting the experimental data points to assumed functional spectral forms using a $\chi^2$ minimization algorithm called CURFIT (Bevington, 1969). The algorithm was used to fit both Maxwellian distributions and $\kappa$-function distributions. The $\kappa$-function distribution, first applied by Vasyliunas (1968) to space plasma measurements, has the functional form for differential flux

$$j(E) \quad \frac{n}{(2mE_0)^{\frac{1}{2}}(\pi\kappa)^{\frac{3}{2}}} \frac{\Gamma(\kappa+1)}{\Gamma(\kappa-\frac{1}{2})} \frac{E/E_0}{(1+E/\kappa E_0)^{\kappa+1}}$$

where $n$ = number density, $E_0$ = most probably energy, and $\kappa$ is the spectral index. An additional derived quantity is the mean, or effective energy

$$E_m = \frac{3}{2} E_0 \left(\kappa - \frac{3}{2}\right),$$

and correspondingly the mean or effective temperature $T_m = E_m/k$. The $\kappa$-function resembles a Maxwellian distribution at low energies but possesses a non-Maxwellian high-energy "tail" with a power-law dependence at high energies. The $\kappa$-function distribution has proved to be a useful description of observed space plasma distributions which are often non-Maxwellian. For the present data, it was found that in most cases the $\kappa$ distribution resulted in a better fit (smaller $\chi^2$) to the data points than did the Maxwellian distribution.

The Type I bow shock electron flux events displayed densities and mean temperatures in the ranges $2\text{–}4 \times 10^{-3}$ cm$^{-3}$ and $1.7\text{–}2.8 \times 10^{6}$ K, respectively. The lower-intensity Type II events were more difficult to fit to spectra because of the very low counting rates and corresponding poor statistics. However, those spectra when fitting could be accomplished successfully resulted in densities and mean temperatures in the ranges $0.5\text{–}2 \times 10^{-3}$ cm$^{-3}$ and $1.0\text{–}1.3 \times 10^{6}$ K ($E_m$ = 90–120 eV), respectively.

A spectrum of a Type III lunar terminator event is shown in Fig. 3. These data were from the event centered at 1220 U.T. on May 20, 1971 (Day 140) (see Fig. 2). The data points and statistical error bars are shown, and the dotted line is the $\kappa$-function fit to the data points. The distribution is described by the parameters $n = 10^{-3}$ cm$^{-3}$, $T_m = 2.6 \times 10^{6}$ K ($E_m$ = 240 eV) and $\kappa = 2$. These values are typical for the Type III events studied. In terms of total electron flux to the lunar surface,

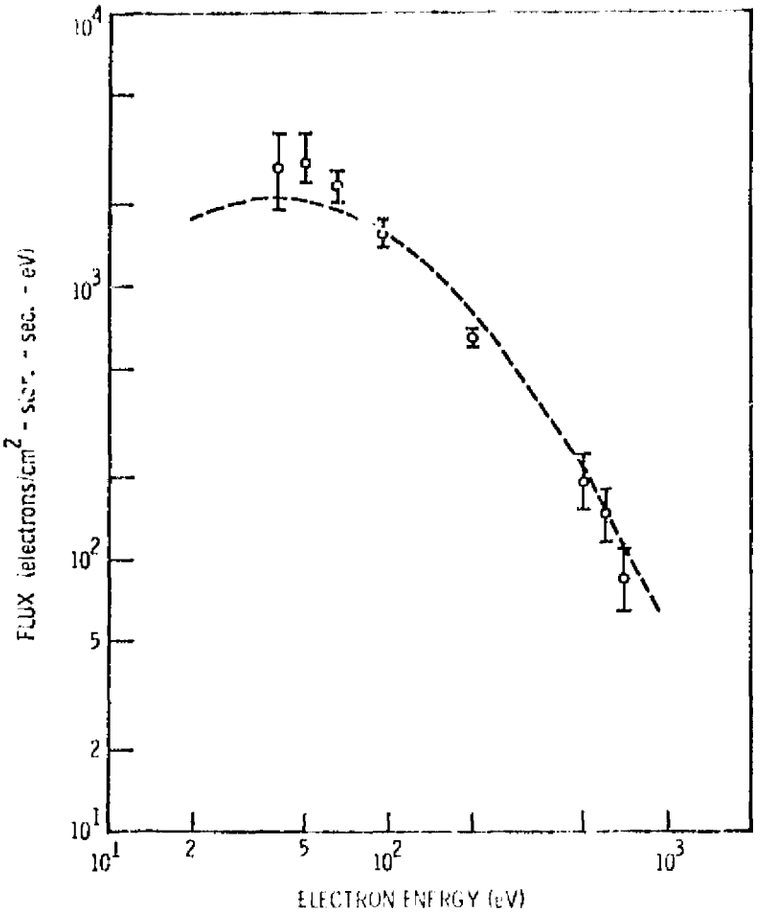


Fig. 3. Electron spectrum of a Type III electron flux event from 1220 U.T. on May 20, 1971 (Day 140). The dotted curve is a $\kappa$ function fit to the data points with the parameters $n = 10^{-2}$ cm$^{-3}$ and $E_m = 240$ eV.

the lunar nightside events represent fluxes ranging from $10^{4}$ electrons/cm$^{2}$ sec (the lower limit of detectability of the CPLEE instrument) to over $10^{7}$ electrons/cm$^{2}$-sec.

In summary, three distinct types of electron flux events at the nightside lunar surface have been identified. The Type I events are electrons that have propagated upstream from the earth's bow shock. Lower intensity Type II events are seen to occur sporadically throughout the lunar night with no dependence either upon the IMF direction, $Kp$, or upon the distance from the lunar terminator. Higher intensity Type III events are seen to be strongly correlated both with distance from the lunar terminator and with $Kp$. In the next section we discuss possible origins of the Type II and Type III events.

## III. Discussion

We proceed upon the assumption that the source of the Type II and Type III electrons is ultimately the solar wind and inquire as to what processes might account for the appearance of these electrons at the lunar nightside surface. The solar wind electron distribution at low energies can be characterized as a Maxwellian distribution with $N_e \approx 5\,\text{cm}^{-3}$ and $T_e \approx 10^5$°K (Montgomery *et al.*, 1968). If this were indeed the case, there would be insufficient electron flux in the energy range 40–700 eV to account for any but the weakest of the Type II events, even assuming a mechanism to scatter them to the lunar night surface with 100% efficiency. However, the measurements of Montgomery *et al.* (1968) also show a high-energy non-Maxwellian "tail" in the solar-wind electron spectrum that becomes significant at energies above 70 eV. (See Fig. 2 of their paper.) The high-energy tail of the solar-wind electron distribution has also been observed by Anderson *et al.* (1972) with detectors on the lunar orbiting Particles and Fields Subsatellite. The energy range covered in that experiment was 520–15 keV. As the subsatellite traversed the solar-wind cavity, it was found that electrons in the energy ranges 0.52–0.58 keV and 1.87–2.08 keV showed a marked decrease in the shadow, while those with energies 5.5–6.5 keV were essentially unaffected by the presence of the moon and cavity, except for particle shadowing effects based on single particle trajectory calculations. Based on these data Anderson *et al.* (1972) argued that electrons with energies above between 2 and 5 keV were decoupled from the solar-wind fluid and had free access to the cavity, whereas lower energy electrons undergo some form of collective interactions and are partially excluded from the cavity. We note that the typical flux at 500 eV for a Type III event ($\sim 2 \times 10^7$ electrons/cm$^2$-sec-ster eV) is of the same order as the flux of 520–580 eV electrons observed inside the cavity by the Particles and Fields Subsatellite (PFS) (see Anderson *et al.*, 1972; Figs. 3 and 4). We argue then that PFS 520–580-eV electron fluxes are a mixture of the types of electron flux events observed by CPLEE, with the Type III events being the dominant contribution near the terminators.

A word of caution is in order here concerning comparison of the PFS and CPLEE observations. First, the observations overlap at only one point of the overall energy spectrum ($\sim$ 500 eV) and, second, the time scale of observations is vastly different. Whereas the PFS completes a cavity transit in about 1 hr, the CPLEE instrument at a fixed location on the lunar surface spends about 14 days in the cavity.

The observations of Montgomery *et al.* (1968) and Anderson *et al.* (1972) discussed above show that there is sufficient electron flux in the high energy tail of the solar-wind electron spectrum to account for the Type II and Type III electron flux events, given that a mechanism exists to decouple the higher energy electrons from the solar wind fluid and allow them to penetrate into the cavity. We shall return to this point later.

Measurements with the lunar orbiting spacecraft Explorer 35 have shown that the moon possesses no significant large scale permanent dipole magnetic field and that no bow shock exists upstream of the moon (Colburn *et al.*, 1967; News *et al.*,

ORIGINAL PAGE IS
OF POOR QUALITY

1967). Plasma observations by Lyon *et al.* (1967) showed an absence of solar wind ions in the downstream cavity with boundary locations and flux decreases consistent with geometrical shadowing of an aberrated solar wind with a finite temperature. The magnetic signature of the solar-wind cavity was observed by both Explorer 35 (Colburn *et al.*, 1967; Ness *et al.*, 1968) and by the Apollo 15 Particle and Fields Subsatellite (Russell *et al.*, 1973) and was found to have the following features: (1) unperturbed interplanetary field on the lunar dayside, (2) a penumbral decrease in magnetic field intensity, and (3) an umbral increase in the magnetic field intensity.

Based on these observations Michel (1968) has presented a hydromagnetic model of solar-wind flow past the moon wherein the moon acts as a perfect absorber of solar-wind particles on the dayside and carves a downstream cavity in the solar-wind flow. In the model, the solar-wind flows transversely into the cavity at the magnetoacoustic velocity, rarefaction waves are formed at the lunar limb and propagate outward, and weak downstream trailing shocks form where the cavity closes. The observed penumbral magnetic field decreases would be coincident with the rarefaction wave region where the plasma density is decreasing and the umbral increases would be a consequence of the requirements of pressure balance. However, both satellites have also observed transient enhancements in the magnetic field strength exterior to the penumbral decrease region, and these enhancements have variously been interpreted as compressional disturbances (Siscoe *et al.*, 1969) or as lunar limb shocks (Schwartz *et al.*, 1970). The penumbral increases are not predicted by the hydromagnetic theory. Various authors have proposed models of these disturbances based on such sources as single particle interactions as the solar-wind grazes the lunar limb, interactions with locally induced eddy currents or remnant magnetization regions, and interaction with the lunar photoelectron layer. For a discussion of these various models the reader is referred to the review paper by Schubert and Lichtenstein (19[illegible] and references therein.

The experimental data from Explorer 35 and the Apollo 15 PFS discussed above show that the bulk of the solar wind behaves as a fluid and is excluded from the downstream cavity. However, solar-wind electrons with energies above a few kiloelectron volts are decoupled from the solar-wind fluid and penetrate into the cavity with little or no attenuation. If it is postulated that electrons in the energy range observed by CPLEE (40–700 eV) are at least partially decoupled, then their appearance in the solar-wind cavity at reduced intensity would be a natural consequence. This would explain the Type II events, whose intensity is constant throughout the lunar night. The sporadic nature of the events would then be a reflection of either the nature of the solar-wind source or of a temporally varying decoupling mechanism. However, the presence of the Type III events, whose intensity is a maximum at or near the lunar terminators suggests that there is an additional decoupling and/or scattering mechanism at or near the terminators which is a direct consequence of the interaction of the solar wind with the lunar body. One possibility is that processes act in the rarefaction region where the solar wind is expanding into the cavity to furnish the required mechanism.

ORIGINAL PAGE IS
OF POOR QUALITY

Such processes, however, would have to be localized near the terminators. If they were continuously active along the region downstream, then one would expect to see events with intensities typical of Type III events throughout the cavity, which is clearly not the case. Another possibility is that the required decoupling and/or scattering mechanism originates in the penumbral magnetic field increases which, as previously stated, have been interpreted as limb compressional disturbances or limb shocks. This interpretation is consistent with the localization of Type III events near the terminators and their correlation with *Kp*. However, studies of the locations of limb magnetic field perturbations with respect to lunar longitude by Sonett and Mihalov (1972) have shown that no such perturbations are regularly observed over the Apollo 14 site. This does not, however, rule out the possibility of weaker perturbations which were not observed by Explorer 35.

These lunar night flux events, although weak in magnitude compared to sources such as the direct solar wind, magnetosheath, and plasma sheet, are nonetheless significant in view of the fact that lunar photoelectrons are not available to provide a return current. Consequently, these electrons should be capable of affecting the lunar nightside surface potential. Theoretical calculations of Manka (1973) based on plasma probe theory result in a value of $-38$ volts for the lunar nightside surface potential when the moon is in the solar wind. Experimental measurements of positive ion fluxes to lunar night surface by the ALSEP/Suprathermal Ion Detector Experiment (SIDE) (Freeman and Ibrahim, 1974) indicate that the lunar nightside potential is actually considerably higher, on the order of a few hundred volts. We suggest therefore that the lunar night electrons flux events, with mean energies in the range of 100–200 volts, are responsible for driving the lunar surface potential to the large negative values inferred by the SIDE measurements. We note that the measured ion densities were in the range 0.05 ions/cm$^3$, which would be of the correct order to provide flux balance to the lunar surface.

In summary, we have identified three distinct types of electron flux events which impact the nightside lunar surface. Two of these were shown to be a result of lunar–solar-wind interactions. We propose that solar-wind electrons in the energy range 40–700 eV are partially decoupled from the solar-wind fluid and are able to penetrate into the downstream cavity, and further that an enhanced source of decoupling and/or scattering is active near the lunar limbs. The effective temperatures of the surface fluxes are in the range of a few hundred electron volts and the total fluxes in the range $10^6$–$10^7$ electrons/cm$^2$-sec. These electrons are likely responsible for the SIDE observations (Freeman and Ibrahim, 1974) of a lunar nightside surface potential on the order of a few hundred volts.

*Acknowledgments*—The author thanks Dr. D. S. Colburn of the NASA/Ames Research Center for supplying Explorer 35 magnetometer data for this study. Patricia H. Reiff, Rice University, provided invaluable assistance in scientific programming.

This work was supported, in part, by NASA contract NAS 9-8851 and NASA grant NSG 07025. The work was performed while the author was a NAS/NRC Senior Postdoctoral Fellow at the NASA/Marshall Space Flight Center.

## REFERENCES


Anderson K. A., Chase L. M., Lin R. P., McCoy J. E., and McGuire R. E. (1972) Solar wind and interplanetary electron measurements on the Apollo 15 subsatellite. *J. Geophys. Res.* 77, 4611–4626.

Bevington P. R. (1969) *Data Reduction and Error Analysis for the Physical Sciences*, Chapter 11. McGraw-Hill, New York.

Burke W. J. and Reasoner D. L. (1972) Absence of the plasma sheet at lunar distance during geomagnetic quiet times. *Planet. Space Sci.* 20, 424–436.

Colburn D. S., Currie R. G., Mihalov J. D., and Sonett C. P. (1967) Diamagnetic solar-wind cavity discovered behind the moon. *Science* 158, 1040–1042.

Freeman J. W., Jr. (1972) Energetic ion bursts on the nightside of the moon. *J. Geophys. Res.* 77, 239–243.

Freeman J. W., Jr. and Ibrahim M. E. (1974) The lunar electric potential and its plasma sheath effects (abstract). In *Lunar Interactions* (editors D. R. Criswell and J. W. Freeman), p. 86–88. The Lunar Science Institute, Houston.

Lyon E. F., Bridge H. S., and Binsack J. H. (1967) Explorer 35 plasma measurements in the vicinity of the moon. *J. Geophys. Res.* 72, 6113–6117.

Manka R. H. (1973) Plasma and potential at the lunar surface. In *Photon and Particle Interactions with Surfaces in Space* (editor R. J. L. Grard), p. 347–361. D. Reidel, Dordrecht.

Michel F. C. (1968) Magnetic field structure behind the moon. *J. Geophys. Res.* 73, 1533–1542.

Montgomery M. D., Bame S. J., and Hundhausen A. J. (1968) Solar wind electrons: Vela 4 measurements. *J. Geophys. Res.* 73, 4999–5003.

Ness N. F., Behannon D. W., Scearce C. S., and Cantarano S. C. (1967) Early results from the magnetic field experiment on Lunar Explorer 35. *J. Geophys. Res.* 72, 5769–5778.

Ness N. F., Behannon D. W., Taylor H. E., and Whang Y. C. (1968) Perturbations of the interplanetary magnetic field by the lunar wake. *J. Geophys. Res.* 73, 3421–3440.

Reasoner D. L. (1975) Observations of low-energy electrons upstream of the earth's bow shock. *J. Geophys. Res.* 80, 187–190.

Reasoner D. L. and Burke W. J. (1972) Characteristics of the lunar photoelectron layer in the geomagnetic tail. *J. Geophys. Res.* 77, 6671–6687.

Russell C. T., Coleman P. J., Jr., Lichtenstein B. R., Schubert G., and Sharp L. R. (1973) Subsatellite measurements of the lunar magnetic field. *Proc. Lunar Sci. Conf. 4th*, p. 2833–2845.

Schubert G. and Lichtenstein B. R. (1974) Observations of moon plasma interactions by orbital and surface experiments. *Rev. Geophys. Space Phys.* 12, 592–626.

Schwartz K., Sonett C. P., and Colburn D. S. (1970) Unipolar induction in the moon and a lunar limb shock mechanism. *The Moon* 1, 7–30.

Scudder J. D., Lind D. L., and Ogilvie K. W. (1973) Electron observations in the solar wind and magnetosheath. *J. Geophys. Res.* 78, 6535–6548.

Siscoe G. L., Lyon E. F., Binsack J. H., and Bridge H. S. (1969) Experimental evidence for a detached lunar compressional wave. *J. Geophys. Res.* 74, 59–69.

Snyder C. W., Neugebauer M., and Rao U. R. (1963) The solar wind velocity and its correlation with cosmic-ray variations and with solar and geomagnetic activity. *J. Geophys. Res.* 68, 6361–6370.

Sonett C. P. and Mihalov J. D. (1972) Lunar fossil magnetism and perturbations of the solar wind. *J. Geophys. Res.* 77, 588–603.

Vasyliunas V. M. (1968) A Survey of low-energy electrons in the evening sector of the magnetosphere with OGO-1 and OGO-3. *J. Geophys. Res.* 73, 2839–2884.